Research Article

Exploring the Role of Structural and Dynamic Complexity in SARS-CoV-2 Nucleocapsid Protein–Heparin Interactions by NMR ☆

Tessa Bolognesi [1,†], Marco Schiavina [1,†], Cristina Ciabini [1], Michela Parafioriti [2], Cristina Gardini [2], Stefano Elli [2], Marco Guerrini [2], Roberta Pierattelli [1,*], and Isabella C. Felli [1,*]

*1 - **Magnetic Resonance Center (CERM) and Department of Chemistry "Ugo Schiff"**, University of Florence, Via L. Sacconi 6, 50019 Sesto Fiorentino, Italy*

*2 - **Istituto di Ricerche Chimiche e Biochimiche G. Ronzoni,** Via G. Colombo 81, 20133 Milano, Italy*

***Correspondence to Roberta Pierattelli and Isabella C. Felli:** roberta.pierattelli@unifi.it (R. Pierattelli), isabellacaterina.felli@unifi.it, felli@cerm.unifi.it (I.C. Felli)*

https://doi.org/10.1016/j.jmb.2025.169437

Edited by Lewis E. Kay

Abstract

Among the structural proteins of SARS-CoV-2, the nucleocapsid (N) protein stands out for its pronounced structural heterogeneity and multifunctionality throughout the viral life cycle. Recent studies have demonstrated that the N protein localizes to the surface of infected and neighboring non-infected cells, by interacting with heparan sulfate in the extracellular matrix. The N protein (419 residues) comprises two folded domains (^{44}NTD^{180} and ^{249}CTD^{361}) interspersed with three intrinsically disordered regions (^{1}IDR1^{43}, ^{181}IDR2^{248}, ^{362}IDR3^{419}). The coexistence of ordered and disordered elements raises a key question: how does this structural heterogeneity influence N's interactions with biological partners? Here we employ high-resolution NMR spectroscopy as the primary technique to characterize the interaction of three N protein constructs (^{44}NTD^{180}, ^{1}NTR^{248}, and ^{1}N^{419}) with heparin-based ligands of increasing complexity. NMR provides atomic level information on the structured NTD domain and on the otherwise difficult to investigate flexible regions. Molecular dynamics simulations further probe the interaction between NTD and short heparin oligosaccharides. Our data reveal a clear correlation between ligand size and binding affinity: longer saccharide chains promote stronger binding. Additionally, the inclusion of intrinsically disordered regions in the NTR construct significantly enhances the interaction compared to NTD, highlighting the functional relevance of structural disorder. Finally, the full-length protein exhibits distinct spectral behavior with the investigated heparin-based ligand, potentially reflecting additional binding contributions and altered dynamics arising from its complex structure. These findings underscore the utility of NMR spectroscopy in elucidating the dynamic, multivalent nature of protein–polyanion interactions, particularly in highly flexible proteins with a modular domain organization.

☆ This article is part of a special issue entitled: 'Advances in NMR (2026)' published in Journal of Molecular Biology.

Introduction

The recent pandemics, originated by the diffusion of the SARS-CoV-2 virus, the agent causing the Covid19 disease, has affected a large portion of the world population. Among those infected, a significant number continue to experience long-term effects of varying severity, which impact their lifestyle [1–4]. Research in the field of SARS-CoV-2 is thus still an active area of research.

While vaccines have significantly contributed to mitigate the devastating effects of the pandemics, the search for efficient drugs to cure the disease is still ongoing. Most of the efforts focused on identifying vaccines and drugs that interfere with the Spike protein or with the Main Protease (3CLpro) [5–7]. The Nucleocapsid (N) protein, despite its importance for the virus life cycle, was not initially considered as a potential target. However, it is one of the viral proteins expressed in higher quantity and with highly immunogenic potential. Indeed, many of the quick COVID-19 swab tests are based on the identification of the N protein [8,9].

The main protein function for the virus consists in genomic RNA encapsulation [10]. However, the protein also engages in interactions with both viral and host proteins to activate gene expression [11,12]. Therefore, the identification of strategies to interfere with the N function would constitute a promising alternative to the ongoing drug discovery initiatives [13]. However, the highly heterogeneous structural and dynamic properties of the protein, constituted by alternating globular domains and highly flexible regions, prevent the use of more established drug-discovery pipelines that generally require a well-defined three-dimensional structure of the target protein to identify small molecules as ligands that perfectly fit in defined protein pockets.

A promising strategy to interfere with the SARS-CoV-2 N protein involves investigating its interactions with linear polyanions [14–17] as well as other molecules [18,19] which share common features to RNA backbones and thus might interfere with one of the key functions of the protein.

Recent studies have demonstrated that the N protein, mainly located inside the virion while packaging RNA, can also be observed on the surface of infected cells, as well as on non-infected neighboring cells, by interacting with heparan sulfate naturally present in the extracellular matrix [15]. Moreover, the presence of N on cell surfaces was recently shown to contribute to the activation of immune reactions through the complement pathway not only aimed at infected cells but also at non-infected ones. The interaction with soluble low-molecular-weight heparins can exert antiviral effects by targeting the N protein, with the added benefit of protecting uninfected cells from complement-mediated cytotoxicity.

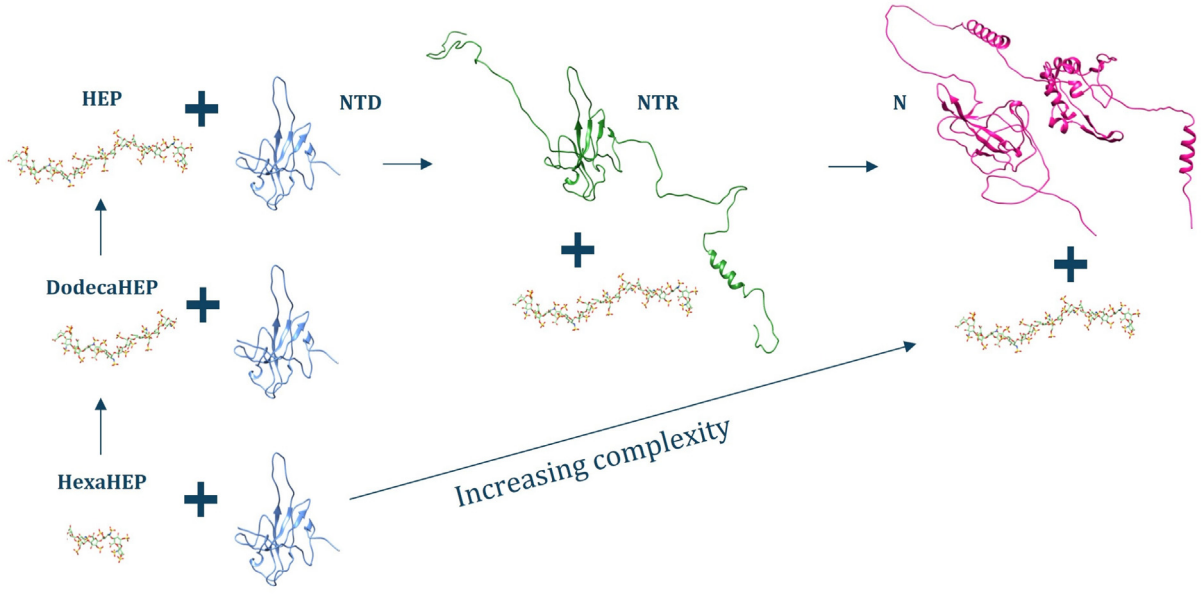

Figure 1. The scheme shows the workflow followed in the present paper. The first studied interaction involves the two smallest constructs (bottom left). A first layer of complexity is introduced by increasing the ligand length (from bottom left to top left). A second layer of complexity is then introduced moving from the study of the interaction of enoxaparin (HEP) with NTD (top left) to the study of the interaction of HEP with the full length N protein (top right). The structural models shown for the different heparin constructs are obtained by manually readapting the 1HPN PDB entry [20,21]. The structure shown for the NTD construct is obtained from the 6YI3 PDB entry [22]. The structural models shown for NTR and N constructs were generated by AlphaFold [23].

Heparin and heparan sulfate are linear, negatively charged polysaccharides belonging to the glycosaminoglycan family. They are composed of repeating disaccharide units consisting of an uronic acid (either β-D-glucuronic or α-L-iduronic acid) 1–4 linked to a α-D-glucosamine (Supplementary Figure 1). The uronic acid can be 2-O-sulfated, while the glucosamine can be 2-N-acetylated or 2-N-sulfated, 6-O-sulfated and more rarely 3-O-sulfated, depending on the animal origin or tissue from which these polyanions are extracted [24–27].

Given the relevance of N–heparin interactions, we aim to elucidate the molecular determinants underlying this binding. High resolution Nuclear Magnetic Resonance (NMR) spectroscopy was employed to investigate how the structural and dynamic properties of both the ligand and the protein modulate the binding. We explored the role of the ligand chain length by studying two size homogeneous heparin oligosaccharide fractions obtained through fractionation of enoxaparin (HEP), a clinically used low molecular weight heparin. In addition we analyzed the full enoxaparin mixture which on average comprises 16 monomeric units. The two fractions correspond to hexa- and dodecasaccharides, hereafter referred to as HexaHEP, and DodecaHEP respectively (Figure 1).

On the protein side, three constructs of increasing complexity of the N protein were investigated. The N protein is inherently modular, featuring three intrinsically disordered regions (IDRs: IDR11–43, IDR2 181–248, and IDR3 362–419) interleaved by two folded domains: the N-terminal domain (NTD, 44–180) and the C-terminal domain (CTD, 249–361) [28,29]. The NTD is composed of seven short β-strands and two short α-helices, forming a compact but dynamically heterogeneous fold. Despite its defined secondary structure elements, the NTD retains a degree of conformational flexibility, particularly in loop regions [22]. Flanking the two folded domains IDR1, IDR2 and IDR3 are disordered and contribute to the overall flexibility of the protein. IDR2, which connects the NTD to the CTD, is enriched in serine/arginine (SR) dipeptides and contains a poly-leucine (PolyL) motif [30]. The SR-rich region in IDR2 is thought to promote dynamic interactions with RNA and other proteins [16,29,31–34], while the hydrophobic nature of the PolyL segment may promote crosstalk with hydrophobic regions of the two globular domains, as well as protein oligomerization [16,31]. IDR2 was also shown to influence the phase separation behavior [34,35]. The CTD forms a compact, α-helix-rich domain that assembles into a highly stable dimer via domain-swapped β-hairpins, contributing to the oligomerization of the N protein [29,36,37].

Here we investigated the interactions using several constructs: the isolated ^{44}NTD^{180}, an extended N-terminal fragment including adjacent disordered regions, ^{1}NTR^{248}, and the full-length protein (N, residues 1–419), as schematically illustrated in Figure 1.

Our findings demonstrate that the length of the ligand and the increasing complexity of the studied N constructs critically influence binding affinity and mode of interaction. Moreover, the heterogeneous structural and dynamic properties of the N protein are crucial to allow the protein to engage in multiple local interactions which contribute to increasing the overall affinity for negatively charged polyanions such as heparin-based ligands.

Results

Interaction of NTD with heparin-based ligands

The NTD construct and its interactions with three different heparin-based ligands, the hexamer (HexaHEP), the dodecamer (DodecaHEP) and enoxaparin (HEP) were investigated acquiring two dimensional ^{1}H–^{15}N HSQC NMR experiments (2D HN) upon addition of increasing amounts of ligand (Table 1). The ligands were obtained from natural products as described in the Materials and Methods section.

The Chemical Shift Perturbation (CSP) for each peak determined by the addition of the ligands was measured, and based on these values graphs were constructed plotting the CSP values against the residue number (Figure 2).

As can be observed in Figure 2, the use of three different heparin-based ligands causes distinct changes in the spectra and it is possible to identify three protein stretches which turn out to be particularly affected: residues T49-F66, R92-D108 (the region that contains the so called “basic finger”) and G164-S176. However, the changes become more pronounced as the length of the polyanion increases with the largest perturbations observed for HEP: in this case changes are already observed for an NTD:HEP ratio of 1:0.1 (Supplementary Figure 2), with more cross peaks

Table 1 Titration points of NTD with HexaHEP, DodecaHEP and HEP monitored through 2D HN NMR experiments. The concentration of NTD used was 90 μM in 25 mM TRIS, 150 mM NaCl buffer at pH 7.3 and T = 298 K.

NTD:HexaHEP	NTD:DodecaHEP	NTD:HEP
0	0	0
0.1 Eq (9.0 μM)	0.1 Eq (9.0 μM)	0.1 Eq (9.0 μM)
0.3 Eq (27 μM)	0.3 Eq (27 μM)	0.3 Eq (27 μM)
0.6 Eq (54 μM)	0.6 Eq (54 μM)	0.6 Eq (54 μM)
1.2 Eq (108 μM)	1.2 Eq (108 μM)	1.2 Eq (108 μM)
3.6 Eq (324 μM)	3.6 Eq (324 μM)	3.6 Eq (324 μM)
6.0 Eq (540 μM)	6.0 Eq (540 μM)	6.0 Eq (540 μM)
12 Eq (1080 μM)		12 Eq (1080 μM)

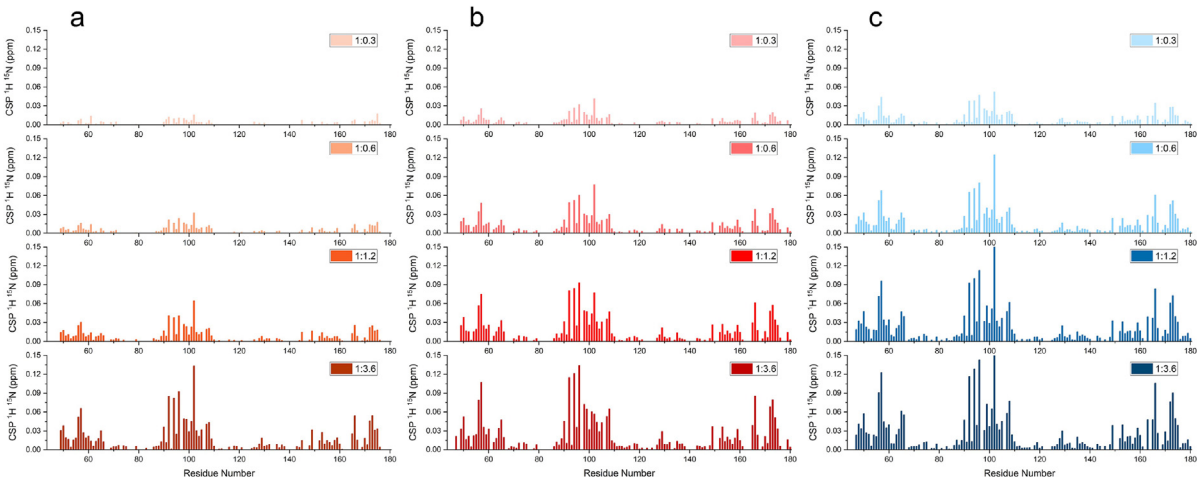

Figure 2. Plots of ^{1}H–^{15}N CSP values against the residue number. Panels **(a), (b)** and **(c)** report the plots of the titration of NTD with HexaHEP, DodecaHEP and HEP at 1:0.3, 1:0.6, 1:1.2, 1:3.6 NTD:ligand molar ratios, respectively.

showing shifts in the spectrum and the shifts themselves being more pronounced.

Even with the medium length heparin-based ligand, the DodecaHEP, the titration shows variations in the spectra at as little as 0.3 Eq of ligand added, although their shift changes are lower than those with enoxaparin. On the contrary, the shorter heparin-based ligand, HexaHEP, causes variations only at higher concentrations. This indicates that longer ligands have higher affinity for the protein.

The increase in affinity with the polyanion length is also stressed by the plots of CSP values against NTD residue numbers at NTD:ligand ratio corresponding to 1:0.6, as shown in Figure 3. The figure clearly highlights the trend described above: a progressive increase in the CSP values moving from the HexaHEP to HEP is evident.

To visualize the protein's most perturbed regions, the CSP values determined in the three titrations (NTD:HexaHEP 1:0.6, NTD:DodecaHEP 1:0.6 and NTD:HEP 1:0.6) were mapped onto the NTD three-dimensional structure [22]. The figure shows that the perturbed regions are similar across the three different titrations, but as the ligand length increases, the interaction capability also rises. However, the effect of DodecaHEP and HEP are closer to one another particularly in the primary binding region, the basic finger, which is similarly affected by the interaction with these two ligands. This observation supports that a correlation exists between heparin-based ligand length and interaction strength (Figure 3).

Figure 4a highlights a region of the spectra showing several peak shifts in the three cases to emphasize the differences between the three NMR titrations. To provide a representative overview, CSP plots at increasing ligand concentrations are shown for three residues (T57, R92, and T166) each located in one of the three most strongly perturbed regions of the protein (Figure 4b). These plots consistently indicate that the interaction increases from HexaHEP to DodecaHEP to HEP, following the same trend across all three regions. To gain qualitative insights into these interactions, K_d values were estimated using the CSP data (reported in the table of Supplementary Figure 3) assuming formation of a 1:1 complex. The K_d values should be intended as "apparent K_d" values which reflect local changes associated to a binding event (rather than the dissociation of a univocally defined binary complex). For this analysis, only well isolated cross peaks that significantly changed their chemical shifts upon addition of the ligand were used. As a representative case, Figure 4c reports the CSP plots and corresponding apparent K_d values for residue I94, confirming an increase in affinity from HexaHEP to DodecaHEP to HEP. A similar trend is observed for other strongly perturbed residues, as shown in Supplementary Figure 3, supporting the general nature of this behavior. These differences correlate with the heparin-based ligand length and demonstrate that the affinity for NTD increases with the polyanion length. This corresponds to an increase of the net charge of these linear polyanions; it is thus interesting to inspect the CSP values as a function of increasing charge concentration (Supplementary Figure 4).

MD simulation of HexaHEP NTD complex

HexaHEP is composed of three (1 → 4)-linked disaccharide units, each containing 2-O-sulfated α-L-iduronic acid (IdoA2S) and 2-N-sulfated, 6-O-sulfated α-D-glucosamine (GlcNS6S) (Scheme 1).

Putative geometries of the complex between HexaHEP and the globular NTD domain have been obtained by docking and molecular dynamic

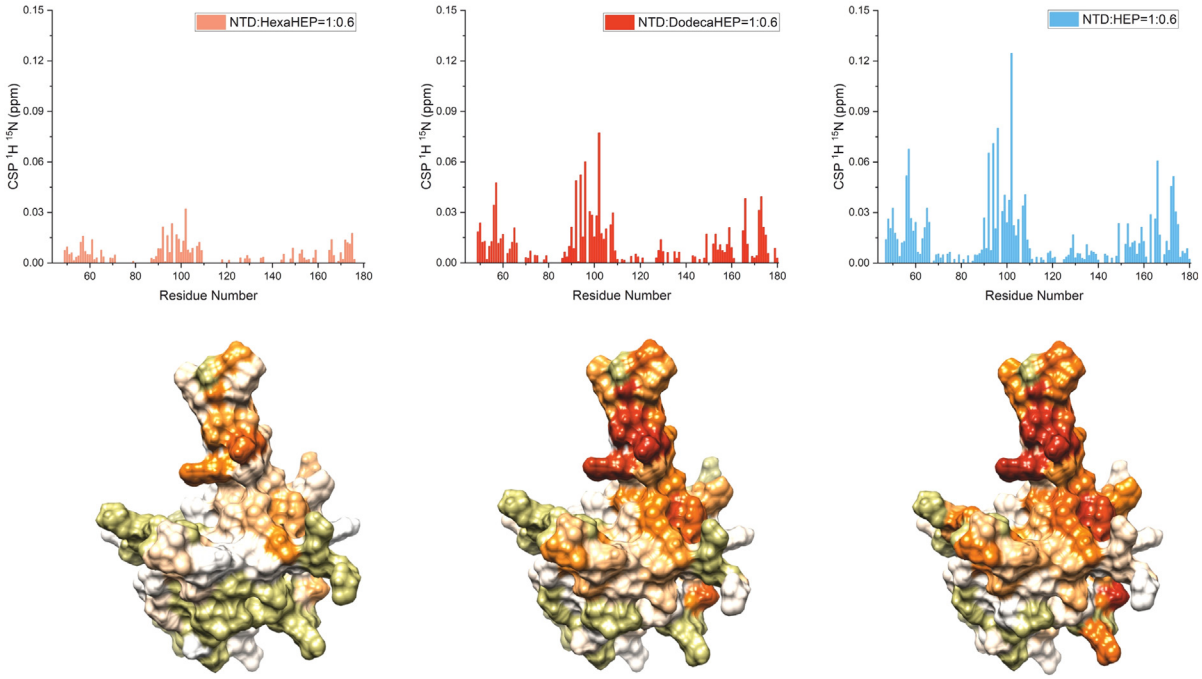

Figure 3. The plots of ^{1}H–^{15}N CSP values against the residue number of NTD at 1:0.6 molar ratio for NTD:HexaHEP (left), NTD:DodecaHEP (middle) and NTD:HEP (right) are reported above. The CSP values are shown on the three dimensional structure of one of the conformers of NTD available in the PDB 6YI3 [22] starting from NTD:HexaHEP (left), to NTD:DodecaHEP (middle) and to NTD:HEP (right). The CSP values are shown according to the values of the average and the standard deviation: 0 $\leq$ CSP < average value (white), average value $\leq$ CSP < 3 $\times$ standard deviation (orange), CSP $\geq$ 3 $\times$ standard deviation (dark red). In all three cases shown in the figure the average value is defined as that of the NTD:HEP interaction, which is taken as the reference for comparison.

(MD) simulation in explicit solvent. An hexasaccharide representing the average composition of heparin (Scheme 1) has been docked on NTD. Three poses (1, 2 and 3) have been selected according to the AutoDock score function (−8.9, −4.9, and +0.38 Kcal mol^{-1}), and their position in the active site of NTD according to the CSP map. Between 100 and 200 ns of MD simulation, the inter-glycosidic conformation of HexaHEP, as well as the epitope map in all the simulated complexes become stable; poses 1, 2 and 3 have been rescored using the MMPBSA free [38] energy of binding (−71.1(3), −50.8(3), −25.4(3) Kcal mol^{-1}). Pose 1 exhibiting the lowest binding energy was therefore selected for accurate contact analysis and reported in Figure 5. The alternative poses 2 and 3 were superposed to pose 1 and reported in Supplementary Figure 5 upon 200 ns of MD simulation. A detailed examination of the contacts between HexaHEP and NTD revealed key interactions that are in good agreement with the experimental CSP (Figure 3 and Supplementary Figure 6). The NTD residues most involved in binding are R92, I94, G96 and K102. Precisely, the guanidinium group of R92 interacts with the carboxylic group of IdoA2S(B) (Scheme 1), maintaining an average distance of approximately 4.4 Å (Supplementary Figure 7) and a persistent hydrogen bond (94% population) between these two groups (Supplementary Table 1). Residue I94 is proximal to GlcNS6S(E); the distance between the anomeric carbon of GlcNS6S(E) and the β-carbon of I94 is around 4.6 Å corresponding to a Van der Waals contact between two apolar surfaces. The backbone NH of G96 interacts with the N-sulfate group of GlcNS6S(E) through a hydrogen bond, with an approximate distance of 4.0 Å between them. The side chain of K102 is located between IdoA2S(B) and GlcNS6S(A). Notably, the distance between the 2-O-sulfate group of IdoA2S(B) and the amine group of K102 decreases from 5.8 Å to 4.2 Å during the simulation time, indicating a stabilization of this interaction mediated by electrostatic and by a persistent hydrogen bond (46% population). Additionally, the interaction between the side chain of K102 and the 6-O-sulfate group of GlcNS6S(A) remains stable at distance around 3.8 Å (Supplementary Figure 7 and Supplementary Table 1).

The protein ribbon in Figure 5 is color-coded (yellow, orange, red) according to experimental CSP, highlighting the agreement between the predicted contacts and the experimental CSP map. The NTD/HexaHEP complex represents one of the possible conformers present in solution, a snapshot that helps us to visualize one of the

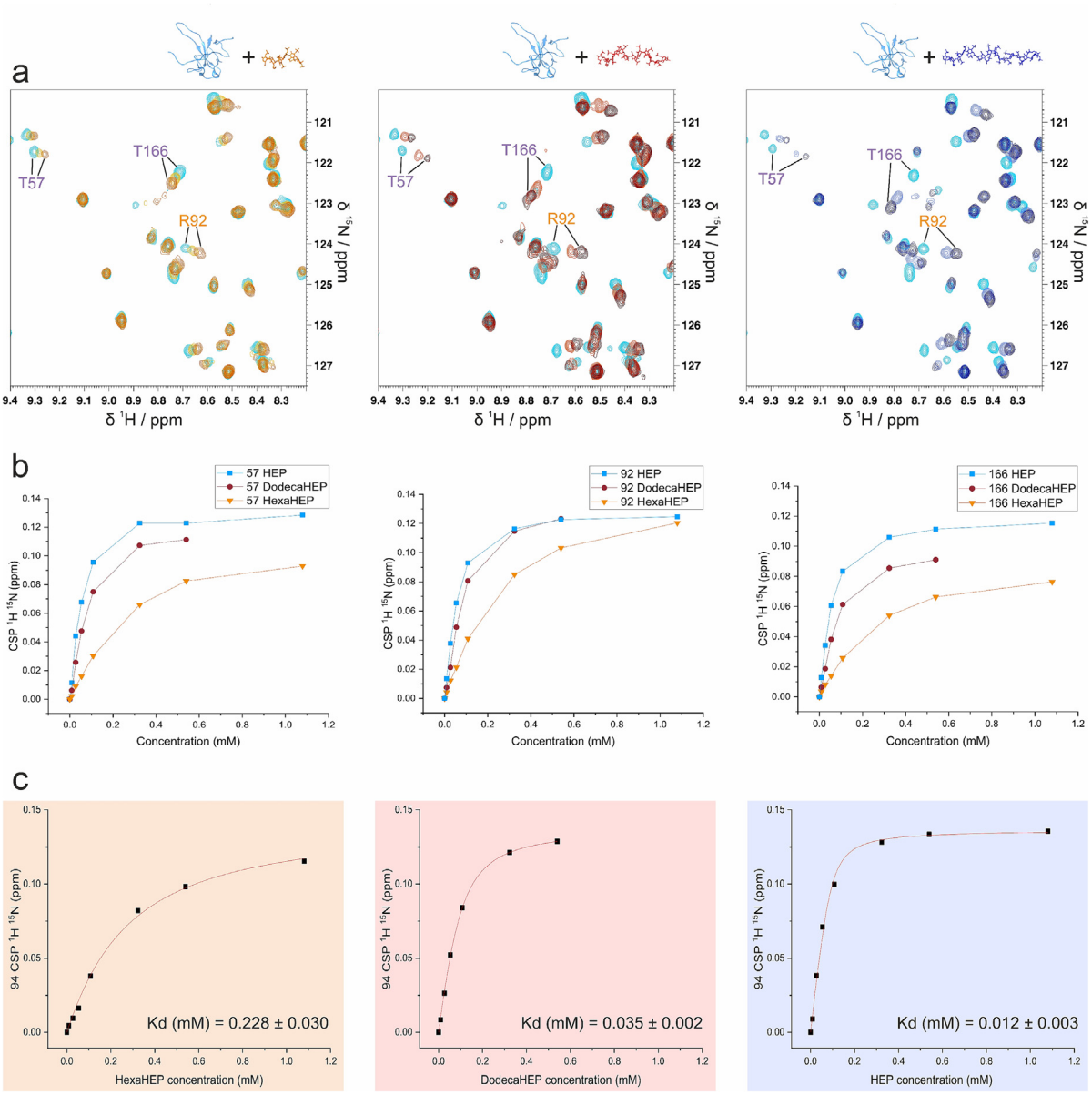

Figure 4. Panel **(a)** shows a zoom on a region of ^{1}H–^{15}N HSQC spectra to highlight how the chemical shift changes sensed by NTD are modulated by the nature of the polyanionic ligand (HexaHEP, DodecaHEP and HEP). The figure shows the spectra of NTD (in light blue), NTD upon addition of 0.6 equivalents of HexaHEP, DodecaHEP and HEP (in yellow, light red, light blue respectively) and 1.2 equivalents (in orange, red and blue). **(b)** The CSP values against ligand concentration of three representative residues T57 (left), R92 (center) and T166 (right) are reported for the three polyanionic ligands investigated: HexaHEP, DodecaHEP and HEP. **(c)** Plots of the CSP of I94 versus increasing concentration of HexaHEP, DodecaHEP and HEP are reported in orange, red and light blue respectively; the data were fitted to extract a value for the apparent K_d assuming a 1:1 interaction. Each graph also reports the obtained apparent K_d value.

possible interaction modes. It also suggests that some level of specificity can be observed in this interaction. Indeed, the globular NTD construct which can adapt its "finger" shape to interact with an RNA fragment [22], is able to host the heparin hexasaccharide. This analysis shows also that the intermolecular forces driving the interaction between NTD and heparin oligosaccharides involve mainly electrostatic interactions, but hydrogen bonds and Van der Waals contacts are also present.

Interaction of NTR with heparin-based ligands

The interaction of the three different heparin-based ligands with the NTR construct, comprising

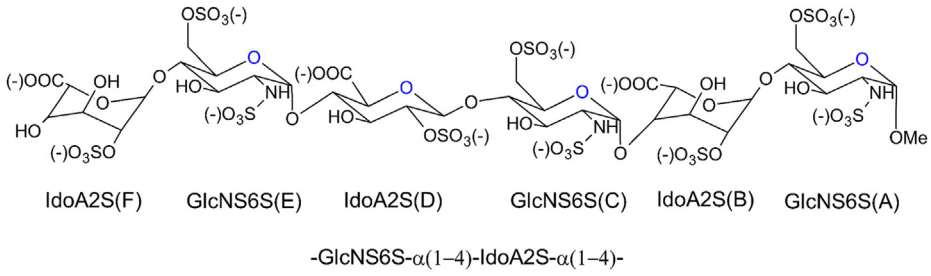

Scheme 1. Molecular structure of HexaHEP oligosaccharide.

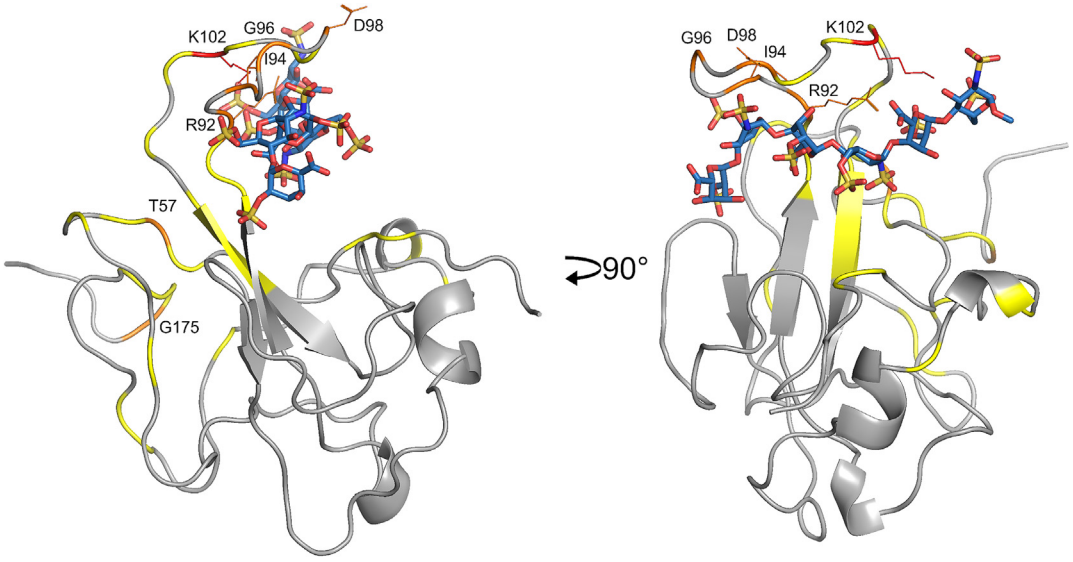

Figure 5. Selected geometry of the HexaHEP-NTD (Pose1) complex after 200 ns of MD simulation. HexaHEP is shown as tubes colored light blue, red, blue and yellow, representing carbon, oxygen, nitrogen and sulfur atoms, respectively. The NTD secondary structure is depicted as ribbon with the following colors: yellow, orange and red indicate CSP (approximated with two decimal digits) up to 0.01, 0.02, and 0.03, respectively.

NTD and the two flanking disordered regions, was then investigated acquiring $^{1}H–^{15}N$ HSQC experiments upon increasing amounts of polyanionic ligand added to the NTR solution (Table 2). The resulting spectra are reported in Figure 6 and the chemical shift perturbations observed as a function of the residue number are reported in Figure 7.

Table 2 Titrations points of NTR with HexaHEP, DodecaHEP and HEP monitored through 2D HN NMR experiments. The concentration of NTR used was 90 μM in 25 mM TRIS, 150 mM NaCl buffer at pH 7.3 and T = 298 K.

NTR:HexaHEP	NTR:DodecaHEP	NTR:HEP
0	0	0
0.1 Eq (9.0 μM)	0.1 Eq (9.0 μM)	0.1 Eq (9.0 μM)
0.3 Eq (27 μM)	0.3 Eq (27 μM)	0.3 Eq (27 μM)
0.6 Eq (54 μM)	0.6 Eq (54 μM)	0.6 Eq (54 μM)
1.2 Eq (108 μM)	1.2 Eq (108 μM)	1.2 Eq (108 μM)
3.6 Eq (324 μM)	3.6 Eq (324 μM)	3.6 Eq (324 μM)
6.0 Eq (540 μM)		

Three key features are observed with respect to the titration performed with isolated NTD:

1. Several cross-peaks disappear upon the addition of longer heparin constructs for the folded domain.
2. The increase in the length of the ligand for the remaining cross peaks causes a lower increase in the observed CSP values for the NTD domain (with respect to when focusing on isolated NTD, Figure 3).
3. Chemical shift perturbations are observed for several cross peaks deriving from the two IDRs.

In particular, while HexaHEP produces mainly chemical shift perturbations, in the DodecaHEP spectra a pronounced line broadening is observed for several cross-peaks deriving from the globular domain (NTD), up to complete disappearance of the cross-peaks. Chemical shift perturbations are

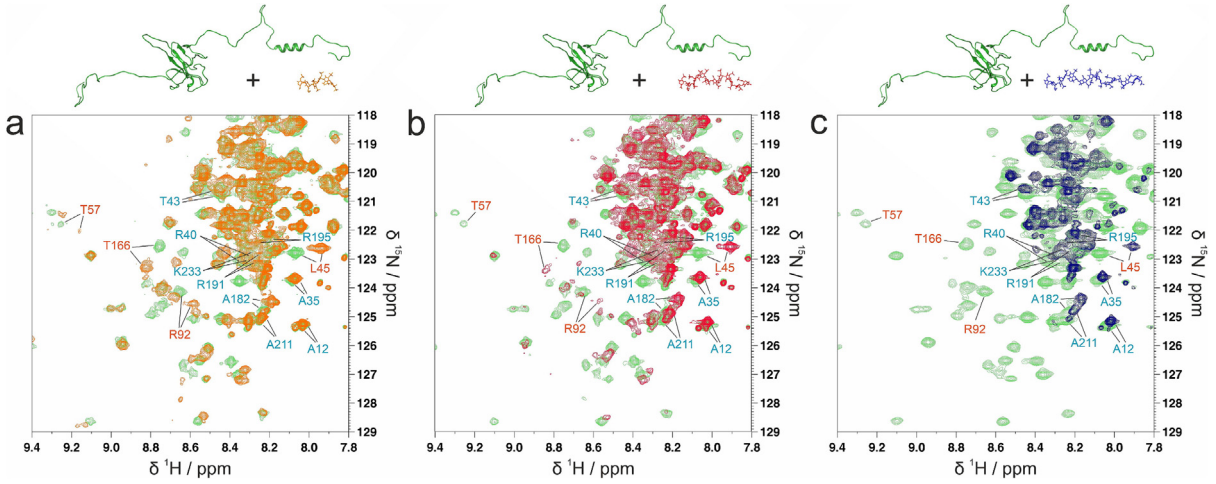

Figure 6. The figure shows a zoom on a region of ^{1}H–^{15}N HSQC spectra of NTR to highlight how different ligands (HexaHEP, DodecaHEP and HEP) produce different changes in the spectra. The figure shows the spectra of NTR (green) and of NTR upon addition of 3.6 equivalents of HexaHEP **(a)**, DodecaHEP **(b)** and HEP **(c)** in orange, red and blue respectively. The assignment of selected cross-peaks belonging to the folded domain and to the IDRs is reported in orange and light blue respectively.

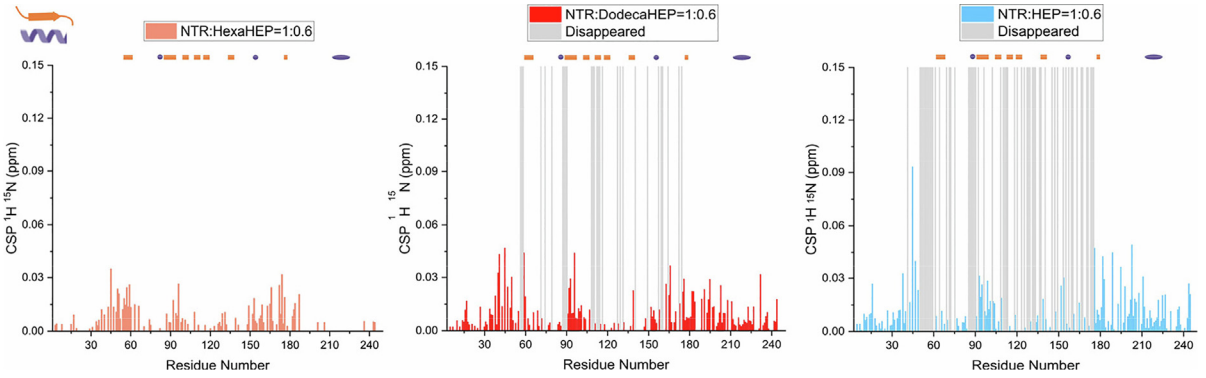

Figure 7. Plots of ^{1}H–^{15}N CSP values against the residue number of NTR at 1:0.6 molar ratio of NTR:HexaHEP (orange), NTR:DodecaHEP (red) and NTR:HEP (blue). The gray bars indicate residues whose 2D HN cross peak is below the detection limit. The orange squares and purple ovals indicate respectively β-strands and α-helix elements present along the sequence.

instead observed for most of the cross-peaks deriving from the two IDRs present in the NTR construct.

Moving to HEP this trend becomes more evident, with a further increase in CSPs for cross-peaks of residues within the IDRs and with a higher number of disappearing peaks deriving from residues belonging to NTD. The latter are mainly concentrated in regions previously identified as the primary CSP sites in the NTD-oligosaccharide interactions.

Importantly, the CSPs observed for peaks belonging to the IDRs (highlighted in light blue in Figure 6) demonstrate the importance of these flexible arms in taking actively part in the interaction. Indeed, positively charged residues, which are highly abundant within the most perturbed disordered regions (4 positively charged residues in the 32–41 stretch (40%) and 6 between residues 177 and 206 (60%) [30]), can act as recruiting sites for negatively charged ligands. These observations suggest that the presence of the flanking IDRs significantly alters the binding mode increasing the interaction capability of NTR with HEP.

One key observation is related to the distribution of CSPs in relation to ligand length. With shorter oligosaccharides like HexaHEP, the CSPs are more evenly spread across both the structured NTD and the disordered regions. This balanced

distribution suggests that the IDRs actively contribute to the binding process, possibly competing with the NTD for ligand interaction. However, as the length of the ligand increases, a distinct effect in this interaction pattern emerges.

For instance, the pronounced disappearance of peaks associated with the NTD upon DodecaHEP interaction is associated with a concomitant increase in the CSPs within the IDRs. This observation implies that longer ligands may interact simultaneously with both structured and disordered regions, potentially modulating their local interaction profile in a length-dependent manner. In the case of HEP, the further loss of NTD signals and the broader distribution of CSPs within the IDRs, support the idea that flexible and disordered regions can easily adapt to interact with complex ligands, establishing more extensive and structurally distinct local interactions. Based on these observations, it is plausible to propose that the interaction between NTR and its ligands is not solely defined by the structured NTD but is also influenced by dynamic and flexible IDRs. These disordered regions, characterized by their positive charges and conformational adaptability, may contribute to expand the overall binding surface, reduce exclusive reliance on the NTD and promote a synergistic binding effect. Consequently, longer ligands function as multivalent compounds, establishing multiple simultaneous contacts with both structured and disordered domains.

How important is the electrostatic contribution to the interaction?

HEP, the longest heparin-based ligand displaying the strongest interaction with NTD and NTR was chosen to study how the ionic strength modulates the interaction. NMR experiments to monitor the interaction were thus repeated at higher ionic strength (25 mM TRIS, 450 mM NaCl, pH 7.3, “high-salt” conditions) and compared to previous results (25 mM TRIS, 150 mM NaCl, pH 7.3, “low-salt” conditions). CSP values observed upon this increasing salt concentration are reported in Supplementary Figure 8 and show minor general changes as well as selected regions of NTR with more pronounced variations, possibly due to weak intramolecular interactions that are modulated by the salt concentration.

A comparison of the NTD spectra presented in Figure 8 reveals distinct effects between the two sample conditions: the spectrum obtained in “low-salt” buffer displays more pronounced chemical shift perturbations, whereas the spectra in high-salt buffer show only minimal changes. This observation aligns with the known effect of increased ionic strength, where the elevated salt concentration screens electrostatic interactions, thereby reducing their contribution to the observed binding effects.

A similar behavior is observed also for the NTR construct that even in these conditions, displays a higher affinity towards HEP with respect to NTD but also a reduced affinity if compared to the titration performed with a lower salt concentration (Supplementary Figure 9).

Taken together, the results indicate that the primary driving force of the interaction is electrostatics. Indeed, most of the residues involved in this interaction, both in the folded domain and in the IDRs, are characterized by a net positive charge in the buffer conditions used in this work.

Although the “high-salt” conditions partially weaken the interaction, they do not abrogate it completely. Instead, they enable the study of a

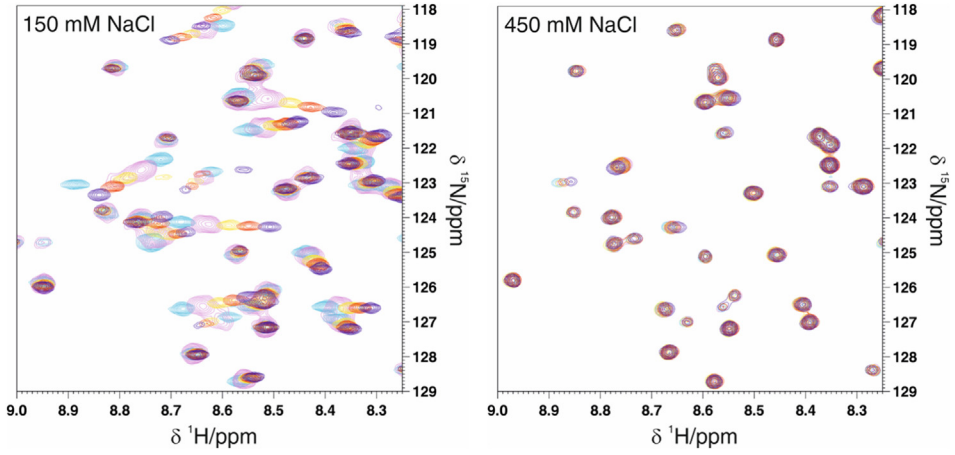

Figure 8. The figure shows on the left the HN-HSQC spectra of the NTD construct upon the addition of 1:0, 1:0.3, 1:0.6, 1:1.2 and 1:6.0 equivalents of HEP in light blue, pink, yellow, orange and blue respectively in the so-called “low salt concentration” conditions (25 mM TRIS 150 mM NaCl pH 7.3). On the right the results of an analogous titration in the so-called “high salt concentration” conditions (25 mM TRIS 450 mM NaCl pH 7.3) is reported for comparison.

more complex and otherwise unstable protein construct: the entire full length Nucleocapsid protein (N).

The full-length nucleocapsid protein (N)

N is composed of 419 amino acids and is known to form dimers in solution [31,39,40]. With respect to NTR, N is characterized by the presence of an additional domain (CTD) and a third disordered linker, IDR3.

This structural heterogeneity is also reflected in the NMR observables. We have previously described the changes of NMR features when moving from NTD to NTR [42].

Comparing instead the fingerprint of NTR and N through 2D HN-based spectra (Figure 9), the two protein constructs present very similar features: in both spectra most of the peaks of the first globular domain can be recognized and are almost superimposable, the peaks belonging to the first two IDRs are present and in very similar positions as well. On the other hand, the central region of the spectrum of N presents a superior number of peaks ascribable to the presence of the third disordered linker, IDR3. Instead, cross peaks indicating the presence of the second C-terminal folded domain (CTD) are not present in our experimental conditions.

Given these spectral features, we thus combined ^{1}H- and ^{13}C-detected experiments [41] to primarily assign the third intrinsically disordered region (IDR3) in the context of the N protein and to confirm the previously obtained assignments of the other two IDRs. The assignment of the folded domain, whose peaks were invisible in the 3D experiments, was instead confirmed by comparing the 2D HN spectra of N with those of NTR [30,42].

With the available chemical shift values of IDR3 (BMRB 53339) it was possible to confirm its disordered nature in solution as demonstrated by the secondary structure propensity (SSP) plot (Supplementary Figure 10).

With all this information, the interaction of N with HEP was followed through ^{1}H–^{15}N HSQC NMR spectra.

The results of the titrations for the three different protein constructs with enoxaparin are reported in Figure 10a. The plots reported in Figure 10b present a comparison between the three titrations illustrating different effects on chemical shifts and peak broadening resulting from the same enoxaparin addition (6 Eq). The NTD shows the smallest variation in terms of chemical shift perturbations, while NTR exhibits the strongest perturbation for the same amount of HEP added.

The picture becomes less straightforward when comparing NTR to the full-length N protein, which seems to have intermediate CSP values compared to NTD and NTR. However, many more signals are broadened beyond detection with respect to those in NTR. This may be due to the larger size of N with respect to the smaller constructs as well as to a possible different

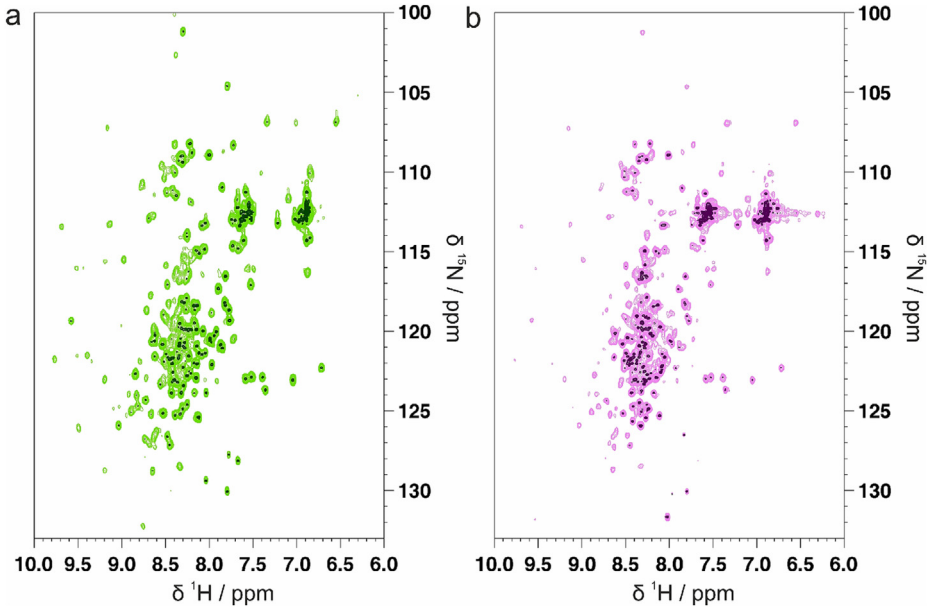

Figure 9. Panel **(a)** and **(b)** show the ^{1}H–^{15}N HSQC spectra acquired on 100 μM NTR and N samples, in green and purple respectively. Each of them is a superposition of the same spectrum with different processing, one optimized for the signal to noise (light green and pink) and the other for the resolution (dark green and purple). Both the samples were dissolved in a buffer containing 25 mM TRIS, 450 mM NaCl at pH 7.3.

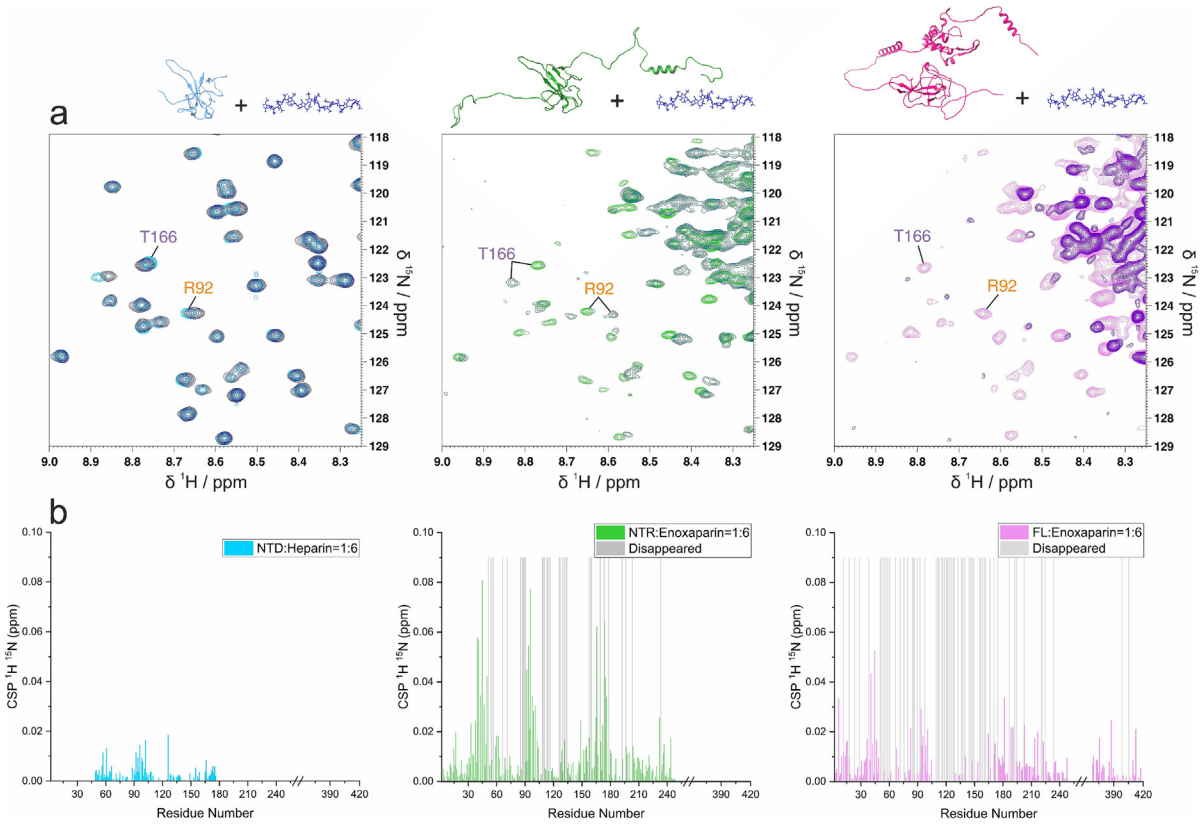

Figure 10. Panel **(a)** shows a zoom on a region of ^{1}H–^{15}N HSQC spectra to highlight how the chemical shift changes sensed by NTD, NTR and N are modulated by HEP. The figure shows the spectra of NTD, NTD upon addition of 6 equivalents of HEP, NTR, NTR upon addition of 6 equivalents of HEP, N and N upon addition of 6 equivalents of HEP in light blue, blue, light green, green, pink and violet respectively. Panel **(b)** shows the chemical shift perturbation plots upon the addition of 6 equivalents of HEP to NTD, NTR and N in light blue, light green and pink respectively. In these latter plots the gray bars represent the residues whose peak disappears upon addition of HEP.

exchange regime for those peaks that are not visible anymore when passing from NTR (fast) to N (intermediate). Worth noting, most of the peaks presenting the highest CSP in NTR and visible also in the N construct are the first ones to vanish in the spectra of N (Figure 11). Consequently, it becomes challenging to definitively conclude whether N interacts more strongly than NTR.

The differences in the interaction with enoxaparin of NTR and N can be related to the increased complexity of the latter that results in a different accessibility to HEP, in particular for the central region (IDR2) which is free in the NTR construct while it is linked to CTD in N. Moreover, a closer inspection of the N spectra also shows the involvement of IDR3 in the interaction. Particularly, residues found in the first portion of IDR3 are the most perturbed ones (K370, K373, K374, K375, A376, T379, Q380 and A381) and most of them are positively charged.

To further characterize this interaction, apparent K_d values for HEP binding were estimated using CSP data of isolated cross peaks, revealing clear differences in affinity among the various constructs. For NTD and NTR, the CSPs could be reliably tracked across multiple residues, allowing for apparent K_d estimations. In contrast, for the full-length N construct, a reliable average apparent K_d could not be determined due to the disappearance or broadening of many peaks upon ligand addition, which complicated a global analysis of the interaction. Nevertheless, by focusing on a residue common to all constructs, namely I94, we were able to extract apparent K_d values: 3.05 ± 0.478 mM for NTD, 0.049 ± 0.012 m M for NTR, and 0.153 ± 0.067 mM for N. These results suggest that the presence of additional regions, particularly disordered ones, significantly modulates the affinity towards HEP.

The observed trends are consistent with the hypothesis that increasing protein complexity influences the interaction with HEP. Indeed, while it becomes challenging to follow residues in the NTD domain across all constructs due to peak loss in the full-length N protein, the IDRs offer a valuable alternative to monitor the interaction.

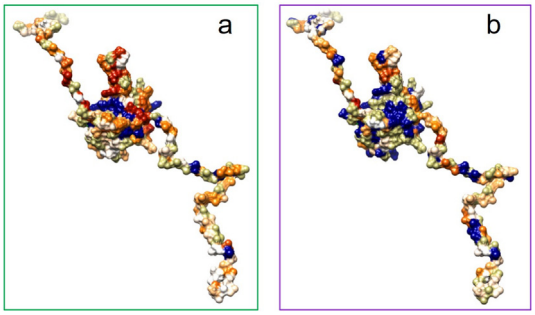

Figure 11. Panels **(a)** and **(b)** show the residues experiencing CSP in the NTR and N constructs upon addition of enoxaparin respectively plotted on the NTR protein frame in a color-coded way. The CSP values are plotted according to the values of the average and the standard deviation: 0 $\leq$ CSP < average value (white), average value $\leq$ CSP < standard deviation $\times$ 3 (orange), CSP $\geq$ standard deviation $\times$ 3 (dark red). Residues colored in blue are the ones whose peak disappears upon the addition of 6 equivalents of enoxaparin.

These regions tend to remain well-resolved and visible even in the full-length protein due to their intrinsic high flexibility also in this construct. This allowed us to determine apparent K_d values for several residues located within IDR1, IDR2, and IDR3, providing additional insights into how these flexible regions contribute to ligand binding (Supplementary Figure 11). They thus play an important role in shaping the overall interaction landscape.

The results are presented in Table 3, with residues from IDR1, IDR2, and IDR3 highlighted in blue, orange, and pink, respectively.

Residues within IDR1 exhibited similar apparent K_d values in both NTR and N, suggesting comparable accessibility. In contrast, residues within IDR2 displayed higher apparent K_d values in N, potentially reflecting reduced accessibility due to their position between two globular domains and proximity to the dimerization domain. IDR3 residues showed the highest apparent K_d values among the three IDRs in N, indicating lower affinity, consistent with its more distal position relative to the primary binding site. These findings underscore the functional relevance of IDRs in modulating enoxaparin binding. While the presence of IDRs generally enhances the overall affinity, their contribution appears context-dependent, influenced by the structural organization and protein configuration.

Table 3 The table shows on the left and right the measured apparent K_d values for different residues found in IDR1 (blue) IDR2 (orange) and IDR3 (pink) for NTR and N respectively.

NTR		N	
Residue	K_d (μM)	Residue	K_d (μM)
12	130 ± 120	12	110 ± 50
15	150 ± 70	15	220 ± 69
32	81 ± 27	35	85 ± 24
35	23 ± 17	37	140 ± 57
40	77 ± 24	201	390 ± 110
205	40 ± 19	217	460 ± 33
209	330 ± 230	223	160 ± 57
232	74 ± 13	240	470 ± 230
243	33 ± 23	248	230 ± 140
		376	740 ± 90
		380	750 ± 100
		381	410 ± 190

Discussion

The interaction studies in which the N protein is involved are very important for the understanding of the function of the protein and of the whole virus. However, the highly heterogeneous structural and dynamic properties of the protein and its dimeric nature significantly complicate the study of the protein in its entirety. Indeed, the whole protein does not crystallize preventing the use of Xray crystallography for the determination of a defined 3D structure. The same structural and dynamic properties make this protein at the low edge of Cryo-EM methods. Studying N in its entirety we show that NMR can provide information on the protein parts that still retain a high degree of flexibility, such as the flexible linkers and the NTD globular domain. Particularly, the NTR region within the full-length protein appears quite similar to when studied in isolation [30]. A notable exception is the PolyL region which is not visible in 3D NMR experiments of N under the studied conditions (observed instead for the NTR construct [30,42]), an aspect that could indicate local interactions within the dimeric constructs as also supported by other studies [31]. The third flexible linker was also identified and results characterized by a slight helical propensity towards its final region. The CTD, the domain responsible for the protein dimerization, which can be investigated in isolation, becomes instead too broad to be detected when part of the complete protein construct [43,44].

With these atomic resolution details in hand the investigation of linear polyanions with different length enables to dissect the driving forces responsible for the interaction among the N protein and heparin. We began by examining the interaction between the smallest and globular protein construct, the NTD domain, and the shortest heparin fragment analyzed, HexaHEP. We then progressively increased the complexity of the systems under investigation, first by extending the length of the heparin polyanion, and subsequently by studying the interaction of

enoxaparin with increasingly complex constructs of the N protein. This progression started from the isolated NTD, incorporated the two flanking IDRs, and ultimately advanced to the full-length N protein.

The results indicate how important local flexibility and dynamics are for the interaction itself. Starting from the NTD domain which, although globular, contains a highly flexible segment, the results show that the basic and dynamic finger region (residues 92–106) is one of the major players in the interaction with heparin polyanions of increasing length, as observed for the interaction with RNA fragments [16,22,45,46]. Docking and MD simulation allow the characterization of the interaction between the shortest hexasaccharide and NTD at atomic resolution, showing several persistent contacts, that are mediated mainly by electrostatic interactions and hydrogen bonds, and that agree with the experimental CSP values. These intermolecular forces establish between the sulfate and carboxyl group of the oligosaccaride and the positive patches of the dynamic finger region residues: R92-D108 of the NTD construct (Figure 5). Van der Waals contacts, such as between I94 and glucosamine (E), are also predicted as short-range interactions. These outcomes are even more exacerbated when considering the NTR construct. In this case the interaction is also promoted by the presence of two highly dynamic and positively charged flanking regions that can help the protein to recruit the negatively charged partners.

The emerging picture is that of a protein constituted by alternating globular and disordered domains which, thanks to its intrinsic flexible nature, can adapt to polyanions (RNA as well as heparin oligosaccharides) of increasing length through an extended ridge of positively charged residues. These residues are located both within the flexible region of the NTD domain and in the adjacent IDRs, all of which are rich in positively charged amino acids and characterized by high local flexibility and disorder. A third IDR, also contributing to the interaction, similarly exhibits marked flexibility and a concentration of positively charged residues. Flexibility thus plays a key role for interactions of N with negatively charged polyanions, another example of “flexible linkers” that have an active role for the overall properties of the protein, well beyond their main task as connectors of globular domains [47,48], a general feature also observed in other IDRs of multidomain proteins as well as for intrinsically disordered proteins (IDPs) [49–54].

Another noteworthy finding from our results is that the binding affinity increases with the length of the heparin ligand, particularly when comparing the NTD construct to the NTR. This trend can be well rationalized by considering that the longer heparin fragments, especially when passing from the HexaHEP to the DodecaHEP, introduce in the picture a greater number of negatively charged units which can interact with a higher number of positively charges residues of the protein; this corresponds to an increase of the number of favorable contacts between ligand and receptor. The enhancement in affinity becomes particularly evident when comparing the interaction between NTD and HexaHEP with that observed between NTR with DodecaHEP (Supplementary Figure 12). In the first case HexaHEP perfectly fits in the major binding site of NTD (Figure 5). In the second one, DodecaHEP continues to form interactions with the flexible finger of the NTD but it can also engage in interactions with the flanking flexible regions thanks to its increasing length. This is a clear example of how local, weak and transient interactions, when simultaneously present in increasing numbers, can collectively enhance the overall binding affinity, as demonstrated in this case. This phenomenon, known as avidity or multivalency, has been previously reported in various contexts involving disordered regions or proteins, including the N protein itself [10,55–61]. Here, we provide experimental data that clearly support this concept, offering atomic resolution insights into which regions of the NTD and of its adjacent intrinsically disordered regions contribute to the progressive increase in affinity for heparin-based polyanions.

However, the structural context of the whole protein must be considered. In the full-length N protein, NTR remains largely visible in the NMR experiments and appears to tumble independently of the central dimerization domain. Interestingly, this full-length construct does not exhibit a further increase in affinity compared to the isolated NTR. This may be due to the NTR being less exposed when incorporated into the full-length protein. In addition, we should also consider that the length of the enoxaparin ligand, (sufficient to interact with the positively charged flexible region composed by the flexible finger of the NTD domain and its flanking regions), is not long enough to engage concomitantly in interactions with a second NTR module present in the dimeric N protein. It would be interesting to investigate whether extending the length of the heparin ligand could result in a further increase in affinity, also considering that the CTD was shown to interact with heparin through low resolution techniques [15]. However, as discussed above, such a modification would likely render the system too complex for high-resolution analysis due to increased molecular weight and a correspondingly slower rotational correlation time upon interaction. Indeed similar studies performed using genomic RNA [59], revealed a pronounced increase in affinity with increasingly large RNA fragments. However, although NMR spectra were used to monitor the overall interaction behavior, the complexity of the system prevented high-resolution structural analysis.

Dimerization of N links together not only the two CTD domains, responsible for the dimerization itself, but it also links in a single entity two NTR units which were shown through our studies to be extensively involved in the interaction with short heparin chains. Extrapolating these findings to interactions of dimeric N with the extracellular heparan sulfate matrix, it is tempting to speculate that the interaction will be even more pronounced as the high positive charge density present in dimeric N will have the possibility to engage in local interactions with the abundant negative charge density on the heparan sulfate extracellular matrix. These interactions could be with a single, longer heparan sulfate chain as well as with different chains that are close to one another, avidly keeping the dimeric N protein linked to the extracellular matrix itself. This process can also influence the properties of the extracellular matrix by modulating its stability/fluidity and affecting the cell microenvironment with possible important biological/biomedical implications [62].

Interestingly a recent paper investigated this topic from a different point of view, using complementary techniques and suggested that the N protein high affinity for cell-surface sulfated glycosaminoglycans, including heparin, is responsible for the identification of N on the surface of infected, as well as non-infected, neighboring cells. This was proposed to activate the immune system not only towards infected cells but also towards neighboring healthy ones. The authors thus proposed a potential role for the extracellular N protein in exacerbating the COVID-19 damages and discussed the possible therapeutic use of enoxaparin to protect uninfected cells from complement-mediated attack [15].

Finally, it is interesting to frame the current results in the more general context of research on SARS-CoV-2. The ability of heparin to interfere with the life cycle of SARS-CoV-2 was initially demonstrated in vitro by observing the inhibition of viral invasion upon administration of exogenous heparin [63,64]. This antiviral effect was initially shown to arise from the competition/interference of heparin with the binding of the SARS-CoV-2 spike (S) protein to heparan sulfate in the extracellular matrix [65]. Indeed, under normal conditions, the S protein binds to heparan sulfate, allowing the virus particles to attach to the cell surface. This initial interaction facilitates the specific engagement of the Angiotensin Converting Enzyme 2 (ACE2) receptor by the tip of the S protein, which is last step required to trigger the fusion between the viral and host cell membranes. The interaction between heparin and the S protein is primarily mediated by electrostatic forces, involving positively charged patches of Arg and Lys residues located on the surface of the S1 subunit and within its receptor binding domain (RBD) [66,67].

Analogously, we now show that the solvent exposed positively charged regions on the N protein sub-domains mediate the interaction with enoxaparin, providing atom-resolved information regarding the key molecular features mediating the attachment of the N protein to the extracellular matrix heparan sulfate. These findings thus reveal interesting molecular details that are expected to stimulate further progress in the design of novel polyanions with increased affinity for the N protein opening novel avenues in the field of drug discovery aimed at interfering with multidomain proteins characterized by a significant level of intrinsic flexibility and disorder.

Conclusions

In conclusion, the reported insights underscore the complexity of the interaction pattern between N and heparin, where both the presence and position of IDRs play a critical role.

An atomic resolution binding interface between heparin oligosaccharide and the globular region of the N protein (NTD) has been proposed. In addition, our NMR data clearly suggest a correlation between ligand length and binding affinity, with longer oligosaccharides showing stronger interactions. Additionally, the presence of IDRs appears to enhance binding capacity, as the NTR construct including disordered segments exhibited more extensive chemical shift perturbations compared to NTD alone. However, while the full-length protein displays distinct spectral behavior, potentially reflecting additional binding contributions from IDR3 and altered dynamics due to its complex structure, a clear description of the interaction involving this intricate modular protein is far from being trivial.

Material and Methods

Protein production

The plasmids encoding the NTD (44–180) and the NTR (1–248) constructs were designed based on the respective homologs of the SARS-CoV-1 virus. The genes for NTD, NTR and the Full Length N protein (N), optimized for *E. Coli*, were inserted into the expression vectors pET28a(+) (Twist Bioscience) and pET29b(+) (Cell Free Sciences) between NdeI and XhoI restriction sites. The NTD construct involves an N-terminal tail (six histidines) removable using TEV (Tobacco Etch Virus) protease. This plasmid was provided by Prof. Almeida (University of Rio de Janeiro). The NTR construct and the FL protein are expressed without the addition of tags useful for purification.

The ^{15}N-labeled NTD was expressed in *E. Coli* strain BL21 (DE3) in M9 minimal medium containing 1.0 g/L ammonium chloride ($^{15}NH_4Cl$) (Cambridge Isotope Laboratories, Tewksbury, MA,

USA). Protein expression was induced over night at an optical density measured at 600 nm (OD_{600}) of 0.7 with 0.2 mM isopropyl-beta-thiogalactopyrano side (IPTG) for 17 h at 16 °C. Cell pellets were resuspended in 50 mM 2-amino-2-(hydroxyme thyl)-1,3-propanediol (TRIS) at pH 8.0, 500 mM sodium chloride (NaCl), 20 mM imidazole ($C_3H_4N_2$), 10% v/v glycerol, and a protease inhibitor cocktail (SIGMAFAST^{tm} tablet). The cells lysis was performed by sonication. The supernatant was cleared by ultracentrifugation for 50 min at 35,000 rpm at 4 °C. The supernatant is collected, filtered (0.2 μm filter) and supplemented with 200 μl of protease inhibitor stock 1000× (SIGMAFAST^{tm} tablet). The cleared supernatant was passed over a Ni^{2+}-NTA HisTrap HP affinity column (GE Healthcare, Chicago, IL, USA), and the His6-Trx-tag was cleaved overnight at 4 °C with 1:10 v/v of TEV protease:protein solution, while dialyzing into fresh buffer composed of 50 mM TRIS at pH 8.0, 500 mM NaCl, and 1 mM dithiothreitol (DTT). TEV protease and the cleaved tag were removed via a second Ni^{2+}-NTA HisTrap HP affinity column. The fractions containing the pure NTD protein were determined by SDS-PAGE and concentrated. Buffer exchange was performed through a PD-10 desalting column (GE Healthcare) or through dialysis, with a final buffer containing 25 mM TRIS, 150 mM sodium chloride (NaCl) at pH 7.3.

Uniformly ^{15}N-labeled NTR and N protein, and uniformly ^{15}N-^{13}C-labeled N protein were expressed in *E. coli* strain BL21 (DE3) following the Marley protocol [68]. The cells were grown in 1 L of Luria Bertani medium at 37 °C until OD_{600} of 1.2. Then, the culture was transferred in 300 mL of labeled M9 minimal medium supplemented with 1.0 g/L $^{15}NH_4Cl$ (Cambridge Isotope Laboratories) and 3.0 g/L of D-glucose (SIGMA). The culture was induced with 0.2 mM IPTG overnight at 15 °C. The solution was then ultracentrifuged at 5500 rpm and 4 °C for 20 min. The cell pellet was then dissolved in 50 mL of lysis buffer (25 mM TRIS pH 8, 1.5 M NaCl, 10% v/v glycerol, 500 μM of a 1000× stock of protease inhibitor cocktail (SIGMAFAST^{tm} tablet), 0.01 mg/ml of DNAase, 0.1 mg/ml of RNAase). The cell lysis was performed by sonication; 50 ml of supernatant is collected after ultracentrifugation of the lysate at 35,000 rpm for 45 min at 4 °C. The latter is then placed into a 10 kDa cut off membrane and dialyzed overnight against 5 L of buffer solution (25 mM TRIS, 150 mM NaCl, pH 7.2) at 4 °C. The protein solution was then loaded onto a HiTrap SP FF 5 mL column and eluted with a high salt buffer (25 mM TRIS pH 7.2 and 1.0 M NaCl). The collected fractions are concentrated and checked by UV_{280} considering a molar extinction coefficient of ε: 26.930 M^{-1} cm^{-1} for NTR and ε: 42.530 M^{-1} cm^{-1} for N. The fractions containing the protein were determined by SDS-PAGE and concentrated.

Protein NMR samples

For the NMR characterization, 500 μL of each protein were placed in a 5 mm tube. All the protein samples were at a concentration of 90 μM and the buffers used were: low salt TRIS (25 mM TRIS and 150 mM NaCl, pH 7.3) and high salt TRIS (25 mM TRIS and 450 mM NaCl, pH 7.3).

The 500 μL samples also contained 10% D_2O, 0,05% NaN_3, 20 μM EDTA and 1 μL Protease Inhibitor Cocktail.

Isolation, purification and characterization of HexaHEP and DodecaHEP oligosaccharides used in NMR experiments

Two types of heparin oligosaccharides were isolated from enoxaparin (Clexane, supplied by Sanofi): the hexamer (HexaHEP) and the dodecamer (DodecaHEP). A batch of enoxaparin was fractionated by size-exclusion chromatography (SEC) to separate fractions based on chain length (Supplementary Figure 13). The fractionation was performed on a Biogel P6 column (5 × 170 cm). Approximately 300–350 mg of sample, dissolved in 5 mL of purified water, was loaded onto the column and eluted with 0.25 M NH_4Cl at a flow rate of 1.8 mL/min. Eluate was collected in approximately 8 mL fractions and UV absorbance was monitored at 210–232 nm. Fractions of interest were pooled and lyophilized. Desalting was carried out using HW40S TSK columns (5 × 85 cm and 2.6 × 60 cm). Samples were eluted with 10% ethanol at flow rates of 5 mL/min (for the 5 × 85 cm column) and 1.4 mL/min (for the 2.6 × 60 cm column). UV absorbance was again monitored at 210–232 nm. Selected fractions were pooled and lyophilized. All isolated fractions were structurally characterized by NMR spectroscopy and high-performance size-exclusion chromatography coupled with triple detection array (HP-SEC/TDA). For the two target fractions, the principal compositional data derived from NMR and the molecular weights determined by HP-SEC/TDA are reported in Supplementary Tables 2 and 3. The isolated fractions were size-homogeneous and exhibited a very low degree of polydispersity (approximately 1), as shown in Supplementary Table 3.

Heparin samples

For the NMR titration three principal types of heparin samples, which differ in the length, were used. The HexaHEP, 6 repetitive units, is the smallest fragment of heparin used. The molecular weight is around 1900 Da; The DodecaHEP, 12 repetitive units, has an intermediate length. The molecular weight is around 3600 Da; Enoxaparin (HEP, as Clexane), is a type of low molecular weight heparin containing fragments with an average molecular weight of around 4500–5000 Da.

- For HexaHEP an initial 18 mM stock solution was prepared, from which all required concentrations for the titration were obtained. The same procedure was followed for DodecaHEP, with an initial stock concentration of 9 mM. The initial stock solution for HEP (enoxaparin) was 22 mM; several stock solutions with different concentrations were then prepared and used for the titrations. All the stock solutions were prepared in the NMR buffer.

Titrations

The three titrations of NTD and the three of NTR with increasingly larger heparin ligands (HexaHEP, DodecaHEP and HEP) were performed under low salt conditions. The buffer used in these titrations was 25 mM TRIS, 150 mM NaCl, pH 7.3. For the titrations of HEP with the three constructs (NTD, NTR and N), a buffer with higher concentration of NaCl (450 mM, high salt condition) was used. This choice was guided by the fact that the full-length protein requires a high salt buffer to remain in solution and prevent aggregation.

All titrations were monitored using 2D ^{1}H–^{15}N HSQC NMR spectra, starting from the reference spectrum of the proteins. Subsequent spectra were acquired on the same sample after the addition of controlled amounts of heparin-based ligands, introduced through small aliquots of different stock solutions at increasing concentrations.

The titration points were decided based on the observed behavior of the proteins (the protein: ligand ratios are reported case-by-case):

- NTD:HexaHEP low salt conditions. 1:0.1, 1:0.3, 1:0.6, 1:1.2, 1:3.6, 1:6.0, 1:12.
- NTD:DodecaHEP low salt conditions. 1:0.1, 1:0.3, 1:0.6, 1:1.2, 1:3.6, 1:6.0.
- NTD: HEP low salt conditions. 1:0.1, 1:0.3, 1:0.6, 1:1.2, 1:3.6, 1:6.0 and 1:12.
- NTR:HexaHEP low salt conditions. 1:0.1, 1:0.3, 1:0.6, 1:1.2, 1:3.6, 1:6.
- NTR:DodecaHEP low salt conditions. 1:0.1, 1:0.3, 1:0.6, 1:1.2, 1:3.6.
- NTR: HEP low salt conditions. 1:0.1, 1:0.3, 1:0.6, 1:1.2, 1:3.6.
- NTD: HEP high salt conditions. 1:0.1, 1:0.3, 1:0.6, 1:1.2, 1:3.6, 1:6.0, 1:12, 1:24, 1:48.
- NTR: HEP high salt conditions. 1:0.1, 1:0.3, 1:0.6, 1:1.2, 1:3.6, 1:6.0.
- FL: HEP high salt conditions. 1:0.1, 1:0.3, 1:0.6, 1:1.2, 1:3.6, 1:6.0, 1:12, 1:24.

NMR experiments

To follow the titrations for all the three constructs 2D HN HSQC experiments were acquired on a Bruker AVANCE NEO spectrometer operating at 900.06 (^{1}H), 226.32 (^{13}C) and 91.20 (^{15}N) MHz equipped with a cryogenically cooled probehead (TCI). All the experiments were conducted at a temperature of 298 K. The acquisition parameters of NMR experiments are reported in Table 4.

IDR3 chemical shift assignment

The assignment of IDR3 in the context of the entire N protein was obtained through a combination of ^{1}H- and ^{13}C-detected experiments [41,42]. The acquired experiments and their most relevant acquisition parameters are reported in Table 5. The experiments were acquired on multiple 100 μM N samples dissolved in 25 mM TRIS, 450 mM NaCl, pH 7.3. All the experiments were acquired at 283 K.

The 2D NMR experiments were acquired on a 28.4 T Bruker AVANCE NEO spectrometer operating at 1200.73 MHz ^{1}H, 301.92 MHz ^{13}C, and 121.67 MHz ^{15}N equipped with a 5 mm cryogenically cooled probehead optimized for ^{13}C-direct detection (CP-TXO). The 3D ^{1}H detected NMR experiments were acquired on a 16.4 T Bruker AVANCE NEO spectrometer operating at 700.13 MHz ^{1}H, 176.05 MHz ^{13}C, and 70.94 MHz ^{15}N frequencies, equipped with a 5 mm cryogenically cooled probehead optimized for ^{1}H direct detection (TCI). (H)CBCACON [71,72] was

Table 4 Acquisition parameters for the recorded spectra.

SALT condition	Construct	Data points		Spectral width (ppm)		Number of scans	Recycle delay (s)
		F2	F1	F2	F1		
Low	NTD:HexaHEP	2048	256	14.6	36.1	8	1.1
	NTD:DodecaHEP	2048	256	14.6	36.1	8	1.1
	NTD:HEP	2048	256	14.6	36.1	8	1.1
Low	NTR:HexaHEP	2048	400	14.6	36.1	24	1.1
	NTR:DodecaHEP	2048	400	14.6	36.1	24	1.1
	NTR:HEP	2048	400	14.6	36.1	24	1.1
High	NTD:HEP	2048	256	14.6	36.1	16	1.1
	NTR:HEP	2048	400	14.6	36.1	32	1.1
	FL:HEP	2048	512	14.6	36.1	24	1.1

Table 5 The table shows the experiments and the most relevant acquisition parameters used to obtain the sequence specific assignment of IDR3 in the context of the full length N protein.

Experiment	Field (^{1}H MHz)	Data points			Spectral widths (ppm)			Number of scans	Recycle delay (s)
		F3	F2	F1	F3	F2	F1		
2D HSQC HN	1200		3500 (^{1}H)	438 (^{15}N)		14.9 (^{1}H)	45.2 (^{15}N)	32	1.1
2D BT HN	1200		8192 (^{1}H)	512 (^{15}N)		19.8 (^{1}H)	45.2 (^{15}N)	128	0.2
2D CON	1200		1024 (^{13}C′)	438 (^{15}N)		19.5 (^{13}C′)	36 (^{15}N)	32	2.1
2D (H)CACO	1200		1024 (^{13}C′)	564 (^{13}C^{ali})		30.1 (^{13}C′)	34.1 (^{13}C^{ali})	16	1.0
2D (H)CBCACO	1200		1024 (^{13}C′)	826 (^{13}C^{ali})		39.4 (^{13}C′)	70.4 (^{13}C^{ali})	32	1.0
3D BT-HNCO	700	2048 (^{1}H)	224 (^{15}N)	46 (^{13}C′)	13.7 (^{1}H)	28.2 (^{15}N)	7.5 (^{13}C′)	32	0.3
3D BT-HN(CA)CO	700	2048 (^{1}H)	96 (^{15}N)	72 (^{13}C′)	13.7 (^{1}H)	28.2 (^{15}N)	7.5 (^{13}C′)	32	0.3
3D CBCACONH	700	2048 (^{1}H)	76 (^{15}N)	74 (^{13}C^{ali})	19.8 (^{1}H)	22.0 (^{15}N)	60.4 (^{13}C^{ali})	16	0.9
3D CBCANH	700	2048 (^{1}H)	76 (^{15}N)	74 (^{13}C^{ali})	19.8 (^{1}H)	22.0 (^{15}N)	60.4 (^{13}C^{ali})	32	0.9
3D (H)CBCACON	700	1024 (^{13}C′)	44 (^{15}N)	64 (^{13}C^{ali})	29.9 (^{13}C′)	34.0 (^{15}N)	60.4 (^{13}C^{ali})	32	1.0

Where BT indicates the application of the BEST-TROSY [69,70] approach.

acquired on a 16.4 T Bruker AVANCE NEO spectrometer operating at 700.06 MHz ^{1}H, 176.03 MHz ^{13}C, and 70.94 MHz ^{15}N frequencies, equipped with a 5 mm cryogenically cooled probehead optimized for ^{13}C direct detection (CP-TXO).

All the 2D-^{13}C detected experiments were acquired in a version optimized for the detection of the highly flexible regions of the protein. Carbon-13 homonuclear decoupling was achieved through the IPAP virtual decoupling approach [73]. 2D-(H)CACO and 2D-(H)CBCACO exploit constant-time evolution in the indirect dimension [72,74].

Pulse lengths and carrier frequencies generally employed for triple resonance experiments were used either for the ^{1}H or ^{13}C detected experiments and are summarized hereafter. The ^{1}H carrier was placed at 4.7 ppm for non-selective hard pulses. ^{13}C pulses were given at 176.7 ppm, 55.9 ppm, and 45.7 ppm for C′, C$^\alpha$ and C^{ali} regions, respectively. ^{15}N pulses were given at 124.0 ppm or 118 ppm in the ^{13}C and ^{1}H detected experiments respectively.

For the experiments acquired at 28.4 T, SURBOP180 and SURBOP90 shapes [75,76] both having a duration of 333 μs were used for ^{13}C band-selective π/2 and π flip angle pulses respectively except for the adiabatic π pulse to invert both C′ and C$^\alpha$ (smoothed Chirp 500 μs, 20% smoothing, 80 kHz sweep width, 11.3 kHz RF field strength). Composite pulse decoupling was applied on ^{1}H (Garp-4 [77]) with an RF field strength of 2.8 kHz. ^{15}N decoupling was achieved through the p5m4 composite pulse decoupling scheme that exploits a series of adiabatic Chirp inversion pulses of 8.4 kHz sweep, 8 ms length, 20% smoothing and 4096 data points for digitization (Crp8.4,8.0,20,4 [78]) with an RF field strength of 0.9 kHz.

For the experiments acquired at 16.4 T, Q5 and Q3 shapes of durations of 300 and 231 μs, respectively, were used for ^{13}C band-selective π/2 and π flip angle pulses except for the adiabatic π pulse to invert both C′ and C$^\alpha$ (smoothed Chirp 500 μs, 20% smoothing, 80 kHz sweep width, 11.3 kHz RF field strength) and the π pulses that should be band-selective on the C$^\alpha$ region (Q3, 900 μs). When needed, composite pulse decoupling was applied on ^{1}H (Waltz-65 [79]) and ^{15}N (Garp-4) with an RF field strength of 2.5 kHz and 1 kHz respectively.

3D ^{1}H detected experiments exploited either the BEST-TROSY [69,70] (3D-BT-HNCO and 3D-BT-HN(CA)CO [80–82]) or the watergate approach (3D-CBCACONH and 3D-CBCANH [80,83]). All the experiments employing the BEST-TROSY approach [69,70] used exclusively shaped proton pulses. PC9 [84] and Reburp [85] shapes of durations of 1831 μs and 1167 μs, respectively, were used for ^{1}H^N band-selective π/2 and π flip angle pulses at 700 ^{1}H MHz.

3D-BT-HNCO, and 3D-BT-HN(CA)CO used semi-constant time in the ^{15}N dimension. 3D-

CBCACONH and 3D-CBCANH experiments used constant time in both the ^{15}N and $^{13}C^{ali}$ dimensions.

All the spectra were acquired, processed, and analyzed by using Bruker TopSpin 4.3.1 software. Chemical shifts were referenced using the ^{1}H and ^{13}C shifts of DSS [86]. Nitrogen chemical shifts were referenced indirectly using the conversion factor derived from the ratio of NMR frequencies [86].

The sequence-specific assignment was performed with the aid of CARA and its tool NEASY [87].

NMR spectral analysis

All the spectra were acquired and processed using the Bruker TopSpin 4.1.3 software. The spectral analysis was conducted with CARA, utilizing its tool NEASY [87]. For each individual construct, we used either the available assignment (BMRB codes: NTD 51620, NTR 50618, 50619) or the one obtained in the context of this work. We accurately positioned the peaks on the reference spectrum and subsequently tracked the signals' chemical shift variations due to interaction by manually adjusting the peaks positions. This allowed us to obtain information about the Chemical Shift Perturbation (CSP) which was then analyzed. More specifically we used the peak lists generated after adjusting the peaks to the NMR spectra acquired upon addition of different amounts of ligand to calculate the CSP values reported in the plots [88]. The CSP values were calculated using the following equation:

$$CSP = \sqrt{\frac{1}{2}\left[\delta_H^2 + (0.1\delta_N)^2\right]}$$

were δ_H and δ_N represent the variations of chemical shift of the ^{1}H and ^{15}N nuclear spins. From the CSP values upon addition of increasing amounts of ligand it was also possible to fit the data assuming a 1:1 interaction mode using the following equation:

$$\frac{\Delta_{obs}}{\Delta_{max}} = \frac{C_p + C_{HEP} + K_d - \sqrt{(C_p + C_{HEP} + K_d)^2 - 4C_pC_{HEP}}}{2C_p}$$

where Δ_{obs} is the observed chemical shift perturbation at the different titration points, Δ_{max} is the maximum value obtained at the end of the titration, C_P is the total protein concentration (NTD, NTR or FL), C_{HEP} is the ligand concentration at the different titration points, and K_d is the dissociation constant. This constant however does not reflect a unique "dissociation event" due to the complexity of the system but rather an "apparent K_d" reflecting local interactions.

The CSP values were then mapped on the protein frame to identify the most perturbed regions of the protein. This was possible using the program CHIMERA which also has the function to plot the CSP values on the structure of a protein.

Molecular docking

The model reported in Scheme 1 was built with GlcNS6S residues in the $^{4}C_1$ chair conformation and IdoA2S residues in the $^{1}C_4$ chair conformation. The conformation of the glycosidic linkages is described by the dihedrals φ_i/ψ_i = ($H1_i$–$C1_i$–O_i–$O4_i$–$C4_i$/$C1_i$–O_i–$O4_i$–$C4_i$–$H4_i$), where the index 'i' runs from 1 to 5. The glycosidic torsion angles φ_i/ψ_i, as well as the orientations of the sulfate groups in GlcNS6S and IdoA2S, were set based on the heparin structure 1HPN from the Protein Data Bank [21] (the φ/ψ dihedral angles are 41/14° and −39/−33° for IdoA2S-GlcNS6S and GlcNS6S-IdoA2S linkages, respectively).

Molecular docking was performed using AutoDock 4.2.3 [89] to generate the geometries of the HexaHEP-NTD complex. The 3D structure of the N-terminal domain of the SARS-CoV-2 nucleocapsid protein (NTD) was extracted from the 'RNA-NTD' complex (PDB ID: 7ACT [22]). The docking grid was centered on the side-chain hydroxyl oxygen of the Y109 residue (CMx = 26.008; CMy = 31.133; CMz = 21.091). The grid size was Lx = Ly = Lz = 100 points with a spacing of $\Delta x = \Delta y = \Delta z = 0.375$ Å. All torsional degrees of freedom in the HexaHEP molecule, except for the glycosidic dihedral angles φ_i/ψ_i, were allowed to be sampled during docking. The receptor was set as rigid. The Lamarckian Genetic Algorithm was used with the following parameters: 100 runs, a population size of 20,000 individuals, a maximum of 5×10^7 energy evaluations and a maximum of 300,000 generations. Fourteen docking solutions were selected based on their binding energy scores (AutoDock 4.2 scoring function, ADT [89]), cluster population and agreement with experimental data. Among these, three complexes were further refined through molecular dynamics (MD) simulations in explicit solvent.

Molecular dynamic simulations

The geometries of the selected HexaHEP-NTD complexes, obtained through molecular docking, were refined via molecular dynamics (MD) simulations in explicit solvent. Topology and coordinate files were prepared using the AmberTools 14 package [90]. The protein and ligand were parametrized with the Amber ff14SB and Glycam06 [91] force fields, respectively. Each complex was solvated by adding a 15 Å layer of TIP3P [92] water molecules in all directions, resulting in an orthorhombic simulation box with edge lengths of approximately 80–90 Å. No counterions were added to the systems. Non-bonded interactions, including electrostatic and van der Waals forces, were truncated at a 12 Å cut-off.

A total of 100,000 steps of energy minimization was performed using NAMD 2.14 [93]. Simulations were run in the NPT ensemble, maintaining constant the number of particles, pressure and temper-

ature. Temperature was maintained at 300 K using a Lowe–Andersen thermostat, and pressure (1.01325 bar) was regulated via the Nosé–Hoover–Langevin piston method. During the initial equilibration phase, harmonic restraints (force constant Ki = 1.0 kcal mol^{-1} $Å^{-2}$) were applied to the solute atoms, which was achieved within 10 ns.

After this stage, the harmonic restraints were removed. Subsequently, each system underwent a 200 ns production MD simulation, that were sampled each 0.1 ns. The trajectory was divided into two phases: the first 100 ns were considered part of the final equilibration, while the remaining 100 ns comprised the production stage. Equilibration was assessed by monitoring the inter-glycosidic dihedral angles $\varphi_i(t)/\psi_i(t)$ until a stable oscillatory behavior was observed.

Binding free energy estimates were obtained using the Molecular Mechanics Poisson–Boltzmann Surface Area (MMPBSA) approach implemented via the MMPBSA.py application [38]. Snapshots from the production phase (between 100 and 200 ns) were analyzed with a sampling interval of 0.2 ns, generating 500 frames.The application VMD [94] was used for the analysis of the MD simulation trajectories. The population percentage of the hydrogen bonds between the HexaHEP and NTD were calculated on the production phase of the MD simulation using the cpptraj application and setting the cutoff distance and angle between the proton donor (Y) and acceptor (X) in the system X:---H-Y, 3.0 Å and 150°, respectively.

CRediT authorship contribution statement

Tessa Bolognesi: Writing – original draft, Investigation, Formal analysis. **Marco Schiavina:** Writing – original draft, Methodology, Investigation. **Cristina Ciabini:** Writing – original draft, Investigation, Formal analysis. **Michela Parafioriti:** Writing – review & editing, Investigation, Formal analysis. **Cristina Gardini:** Investigation. **Stefano Elli:** Writing – review & editing, Investigation, Formal analysis. **Marco Guerrini:** Writing – review & editing, Investigation, Conceptualization. **Roberta Pierattelli:** Writing – original draft, Supervision, Investigation, Funding acquisition, Conceptualization. **Isabella C. Felli:** Writing – original draft, Supervision, Investigation.

Funding

This work was supported by the European Union-NextGenerationEU through the ItaliaDomani PNRR project 'Potentiating the Italian Capacity for Structural Biology Services in Instruct-ERIC' (ITACA.SB, no. IR0000009, CUP B53C22001790006) and by the Italian Ministry of Health project "Hub multidisciplinare e interregionale di ricerca e sperimentazione clinica per il contrasto alle pandemie ed all'antibiotico resistenza" (PAN-HUB 2021-T4-AN-07).

DATA AVAILABILITY

Data will be made available on request.

DECLARATION OF COMPETING INTEREST

The authors declare that they have no known competing financial interests or personal relationships that could have appeared to influence the work reported in this paper.

Acknowledgment

The support of the CERM/CIRMMP center of Instruct-ERIC and of the Italian Ministry for University and Research (MUR, FOE funding) is gratefully acknowledged.

Appendix A. Supplementary material

Supplementary material to this article can be found online at https://doi.org/10.1016/j.jmb.2025.169437.

Received 17 July 2025;
Accepted 8 September 2025;
Available online 11 September 2025

Keywords:
nuclear magnetic resonance;
multidomain protein;
SARS-CoV-2;
heparin;
molecular dynamics simulation

† These authors contributed equally.

References

[1]. Joshee, S., Vatti, N., Chang, C., (2022). Long-term effects of COVID-19. *Mayo Clin. Proc.* **97**, 579–599. https://doi.org/10.1016/j.mayocp.2021.12.017.

[2]. Davis, H.E., McCorkell, L., Vogel, J.M., Topol, E.J., (2023). Long COVID: major findings, mechanisms and recommendations. *Nature Rev. Microbiol.* **21**, 133–146. https://doi.org/10.1038/s41579-022-00846-2.

[3]. Yong, S.J., (2021). Long COVID or post-COVID-19 syndrome: putative pathophysiology, risk factors, and treatments. *Infect. Dis.* **53**, 737–754. https://doi.org/10.1080/23744235.2021.1924397.

[4]. Cervia-Hasler, C., Brüningk, S.C., Hoch, T., Fan, B., Muzio, G., Thompson, R.C., Ceglarek, L., Meledin, R., Westermann, P., Emmenegger, M., Taeschler, P., Zurbuchen, Y., Pons, M., Menges, D., Ballouz, T., Cervia-Hasler, S., Adamo, S., Merad, M., Charney, A. W., Puhan, M., Brodin, P., Nilsson, J., Aguzzi, A., Raeber, M.E., Messner, C.B., Beckmann, N.D., Borgwardt, K.,

Boyman, (2024). Persistent complement dysregulation with signs of thromboinflammation in active long Covid. *Science* **383**, eadg7942. https://doi.org/10.1126/science.adg7942.

[5]. Heidary, M., Kaviar, V.H., Shirani, M., Ghanavati, R., Motahar, M., Sholeh, M., Ghahramanpour, H., Khoshnood, S., (2022). A comprehensive review of the protein subunit vaccines against COVID-19. *Front. Microbiol.* **13**, 927306. https://doi.org/10.3389/fmicb.2022.927306.

[6]. Li, Y., Tenchov, R., Smoot, J., Liu, C., Watkins, S., Zhou, Q., (2021). A comprehensive review of the global efforts on COVID-19 vaccine development. *ACS Cent. Sci.* **7**, 512–533. https://doi.org/10.1021/acscentsci.1c00120.

[7]. Dhaka, P., Singh, A., Choudhary, S., Peddinti, R.K., Kumar, P., Sharma, G.K., Tomar, S., (2022). Mechanistic and thermodynamic characterization of antivirals targeting druggable pocket of SARS-CoV-2 nucleocapsid. *Arch. Biochem. Biophys.* **750**, 109820. https://doi.org/10.1101/2022.03.12.484092.

[8]. Diao, B., Wen, K., Zhang, J., Chen, J., Han, C., Chen, Y., Wang, S., Deng, G., Zhou, H., Wu, Y., (2021). Accuracy of a nucleocapsid protein antigen rapid test in the diagnosis of SARS-CoV-2 infection. *Clin. Microbiol. Infect.* **27**, 289.e1–289.e4. https://doi.org/10.1016/j.cmi.2020.09.057.

[9]. Fox, T., Geppert, J., Dinnes, J., Scandrett, K., Bigio, J., Sulis, G., Hettiarachchi, D., Mathangasinghe, Y., Weeratunga, P., Wickramasinghe, D., Bergman, H., Buckley, B.S., Probyn, K., Sguassero, Y., Davenport, C., Cunningham, J., Dittrich, S., Emperador, D., Hooft, L., Leeflang, M.M., McInnes, M.D., Spijker, R., Struyf, T., Van den Bruel, A., Verbakel, J.Y., Takwoingi, Y., Taylor-Phillips, S., Deeks, J.J., (2022). Antibody tests for identification of current and past infection with SARS-CoV-2. *Cochrane Database Syst. Rev.* **11**, 1465–1858. https://doi.org/10.1002/14651858.CD013652.pub2.

[10]. Zhao, H., Syed, A.M., Khalid, M.M., Nguyen, A., Ciling, A., Wu, D., Yau, W.-M., Srinivasan, S., Esposito, D., Doudna, J.A., Piszczek, G., Ott, M., Schuck, P., (2024). Assembly of SARS-CoV-2 nucleocapsid protein with nucleic acid. *Nucleic Acids Res.* **52**, 6647–6661. https://doi.org/10.1093/nar/gkae256.

[11]. Eltayeb, A., Al-Sarraj, F., Alharbi, M., Albiheyri, R., Mattar, E., Abu Zeid, I.M., Bouback, T.A., Bamagoos, A., Aljohny, B.O., Uversky, V.N., Redwan, E.M., (2024). Overview of the SARS-CoV-2 nucleocapsid protein. *Int. J. Biol. Macromol.* **260**, 129523. https://doi.org/10.1016/j.ijbiomac.2024.129523.

[12]. Wang, W., Chen, J., Yu, X., Lan, H.-Y., (2022). Signaling mechanisms of SARS-CoV-2 Nucleocapsid protein in viral infection, cell death and inflammation. *Int. J. Biol. Sci.* **18**, 4704–4713. https://doi.org/10.7150/ijbs.72663.

[13]. Wu, W., Cheng, Y., Zhou, H., Sun, C., Zhang, S., (2023). The SARS-CoV-2 nucleocapsid protein: its role in the viral life cycle, structure and functions, and use as a potential target in the development of vaccines and diagnostics. *Virol. J.* **20**, 6. https://doi.org/10.1186/s12985-023-01968-6.

[14]. Tino, A.S., Quagliata, M., Schiavina, M., Pacini, L., Papini, A.M., Felli, I.C., Pierattelli, R., (2025). Revealing the potential of a chimaera: a peptide-peptide nucleic acid molecule designed to interact with the SARS-CoV-2 nucleocapsid protein. *Angew. Chem. Int. Ed.* **64**, e202420134. https://doi.org/10.1002/anie.202420134.

[15]. Fahoum, J., Billan, M., Varga, J.K., Padawer, D., Britan-Rosich, Y., Elgrably-Weiss, M., Basu, P., Stolovich-Rain, M., Baraz, L., Cohen-Kfir, E., Kumari, S., Oiknine-Djian, E., Kumar, M., Zelig, O., Mayer, G., Isupov, M.N., Wolf, D. G., Altuvia, S., Wiener, R., Schueler-Furman, O., Rouvinski, A., (2025). Transfer of SARS-CoV-2 nucleocapsid protein to uninfected epithelial cells induces antibody-mediated complement deposition. *Cell Rep.* **44**, 115512. https://doi.org/10.1016/j.celrep.2025.115512.

[16]. Pontoriero, L., Schiavina, M., Korn, S.M., Schlundt, A., Pierattelli, R., Felli, I.C., (2022). NMR reveals specific tracts within the intrinsically disordered regions of the SARS-CoV-2 nucleocapsid protein involved in RNA encountering. *Biomolecules* **12**, 929. https://doi.org/10.3390/biom12070929.

[17]. Schiavina, M., Pontoriero, L., Tagliaferro, G., Pierattelli, R., Felli, I.C., (2022). The role of disordered regions in orchestrating the properties of multidomain proteins: the SARS-CoV-2 nucleocapsid protein and its interaction with enoxaparin. *Biomolecules* **12**, 1302. https://doi.org/10.3390/biom12091302.

[18]. Dang, M., Li, Y., Song, J., (2021). ATP biphasically modulates LLPS of SARS-CoV-2 nucleocapsid protein and specifically binds its RNA-binding domain. *Biochem. Biophys. Res. Commun.* **541**, 50–55. https://doi.org/10.1016/j.bbrc.2021.01.018.

[19]. Kumari, S., Mistry, H., Bihani, S.C., Mukherjee, S.P., Gupta, G.D., (2024). Unveiling potential inhibitors targeting the nucleocapsid protein of SARS-CoV-2: structural insights into their binding sites. *Int. J. Biol. Macromol.* **273**, 133167. https://doi.org/10.1016/j.ijbiomac.2024.133167.

[20]. Khan, S., Gor, J., Mulloy, B., Perkins, S.J., (2013). Corrigendum to “semi-rigid solution structures of heparin by constrained X-ray scattering modelling: new insight into heparin–protein complexes. *J. Mol. Biol.* **425**, 1847. https://doi.org/10.1016/j.jmb.2013.02.028.

[21]. Khan, S., Gor, J., Mulloy, B., Perkins, S.J., (2010). Semi-rigid solution structures of heparin by constrained X-ray scattering modelling: new insight into heparin–protein complexes. *J. Mol. Biol.* **395**, 504–521. https://doi.org/10.1016/j.jmb.2009.10.064.

[22]. Dinesh, D.C., Chalupska, D., Silhan, J., Koutna, E., Nencka, R., Veverka, V., Boura, E., (2020). Structural basis of RNA recognition by the SARS-CoV-2 nucleocapsid phosphoprotein. *PLoS Pathog.* **16**, e1009100. https://doi.org/10.1371/journal.ppat.1009100.

[23]. Varadi, M., Anyango, S., Deshpande, M., Nair, S., Natassia, C., Yordanova, G., Yuan, D., Stroe, O., Wood, G., Laydon, A., Žídek, A., Green, T., Tunyasuvunakool, K., Petersen, S., Jumper, J., Clancy, E., Green, R., Vora, A., Lutfi, M., Figurnov, M., Cowie, A., Hobbs, N., Kohli, P., Kleywegt, G., Birney, E., Hassabis, D., Velankar, S., (2022). AlphaFold protein structure database: massively expanding the structural coverage of protein-sequence space with high-accuracy models. *Nucleic Acids Res.* **50**, D439–D444. https://doi.org/10.1093/nar/gkab1061.

[24]. Lindahl, U., Hook, M., (1978). Glycosaminoglycans and their binding to biological macromolecules. *Annu. Rev. Biochem.* **47**, 385–417. https://doi.org/10.1146/annurev.bi.47.070178.002125.

[25]. Casu, B., Lindahl, U., (2001). Structure and biological interactions of heparin and heparan sulfate, in. *Adv.*

Carbohydr. Chem. Biochem., 159–206. https://doi.org/10.1016/S0065-2318(01)57017-1.

[26]. Rosenberg, R.D., Lam, L., (1979). Correlation between structure and function of heparin. *PNAS* **76**, 1218–1222. https://doi.org/10.1073/pnas.76.3.1218.

[27]. Gallagher, J.T., Lyon, M., Steward, W.P., (1986). Structure and function of heparan sulphate proteoglycans. *Biochem. J.* **236**, 313–325. https://doi.org/10.1042/bj2360313.

[28]. Peng, Y., Du, N., Lei, Y., Dorje, S., Qi, J., Luo, T., Gao, G. F., Song, H., (2020). Structures of the SARS-CoV-2 nucleocapsid and their perspectives for drug design. *EMBO J.* **39**, e105938. https://doi.org/10.15252/embj.2020105938.

[29]. Ye, Q., West, A.M.V., Silletti, S., Corbett, K.D., (2020). Architecture and self-assembly of the SARS-CoV-2 nucleocapsid protein. *Protein Sci.* **29**, 1890–1901. https://doi.org/10.1002/pro.3909.

[30]. Schiavina, M., Pontoriero, L., Uversky, V.N., Felli, I.C., Pierattelli, R., (2021). The highly flexible disordered regions of the SARS-CoV-2 nucleocapsid N protein within the 1–248 residue construct: sequence-specific resonance assignments through NMR. *Biomol. NMR Assign.* **15**, 219–227. https://doi.org/10.1007/s12104-021-10009-8.

[31]. Hernandez, G., Martins, M.L., Fernandes, N.P., Veloso, T., Lopes, J., Gomes, T., Cordeiro, T.N., (2025). Dynamic ensembles of SARS-CoV-2 N-protein reveal head-to-head coiled-coil-driven oligomerization and phase separation. *Nucleic Acids Res.* **53**, gkaf502. https://doi.org/10.1093/nar/gkaf502.

[32]. Bessa, L.M., Guseva, S., Camacho-Zarco, A.R., Salvi, N., Maurin, D., Perez, L.M., Botova, M., Malki, A., Nanao, M., Jensen, M.R., Ruigrok, R.W.H., Blackledge, M., (2022). The intrinsically disordered SARS-CoV-2 nucleoprotein in dynamic complex with its viral partner nsp3a. *Sci. Adv.* **8**, eabm4034. https://doi.org/10.1126/sciadv.abm4034.

[33]. Tayeb-Fligelman, E., Bowler, J.T., Tai, C.E., Sawaya, M. R., Jiang, Y.X., Garcia, G., Griner, S.L., Cheng, X., Salwinski, L., Lutter, L., Seidler, P.M., Lu, J., Rosenberg, G.M., Hou, K., Abskharon, R., Pan, H., Zee, C.-T., Boyer, D.R., Li, Y., Anderson, D.H., Murray, K.A., Falcon, G., Cascio, D., Saelices, L., Damoiseaux, R., Arumugaswami, V., Guo, F., Eisenberg, D.S., (2023). Low complexity domains of the nucleocapsid protein of SARS-CoV-2 form amyloid fibrils. *Nature Commun.* **14**, 2379. https://doi.org/10.1038/s41467-023-37865-3.

[34]. Savastano, A., Ibáñez de Opakua, A., Rankovic, M., Zweckstetter, M., (2020). Nucleocapsid protein of SARS-CoV-2 phase separates into RNA-rich polymerase-containing condensates. *Nature Commun.* **11**, 6041. https://doi.org/10.1038/s41467-020-19843-1.

[35]. Stuwe, H., Reardon, P.N., Yu, Z., Shah, S., Hughes, K., Barbar, E.J., (2024). Phosphorylation in the Ser/Arg-rich region of the nucleocapsid of SARS-CoV-2 regulates phase separation by inhibiting self-association of a distant helix. *J. Bio Chem.* **300**, 107354. https://doi.org/10.1016/j.jbc.2024.107354.

[36]. Zhao, H., Wu, D., Hassan, S.A., Nguyen, A., Chen, J., Piszczek, G., Schuck, P., (2023). A conserved oligomerization domain in the disordered linker of coronavirus nucleocapsid proteins. *Sci. Adv.* **9**, eadg6473. https://doi.org/10.1126/sciadv.adg6473.

[37]. Slavin, M., Zamel, J., Zohar, K., Eliyahu, T., Braitbard, M., Brielle, E., Baraz, L., Stolovich-Rain, M., Friedman, A., Wolf, D.G., Rouvinski, A., Linial, M., Schneidman-Duhovny, D., Kalisman, N., (2021). Targeted in situ cross-linking mass spectrometry and integrative modeling reveal the architectures of three proteins from SARS-CoV-2. *PNAS* **118**, e2103554118. https://doi.org/10.1073/pnas.2103554118.

[38]. Miller, B.R., McGee, T.D., Swails, J.M., Homeyer, N., Gohlke, H., Roitberg, A.E., (2012). *MMPBSA.py*: an efficient program for end-state free energy calculations. *J. Chem. Theory Comput.* **8**, 3314–3321. https://doi.org/10.1021/ct300418h.

[39]. Padroni, G., Bikaki, M., Novakovic, M., Wolter, A.C., Rüdisser, S.H., Gossert, A.D., Leitner, A., Allain, F.-H.-T., (2023). A hybrid structure determination approach to investigate the druggability of the nucleocapsid protein of SARS-CoV-2. *Nucleic Acids Res.* **51**, 4555–4571. https://doi.org/10.1093/nar/gkad195.

[40]. Zhao, H., Wu, D., Nguyen, A., Li, Y., Adão, R.C., Valkov, E., Patterson, G.H., Piszczek, G., Schuck, P., (2021). Energetic and structural features of SARS-CoV-2 N-protein co-assemblies with nucleic acids. *Iscience* **24**, 102523. https://doi.org/10.1016/j.isci.2021.102523.

[41]. Schiavina, M., Bracaglia, L., Bolognesi, T., Rodella, M.A., Tagliaferro, G., Tino, A.S., Pierattelli, R., Felli, I.C., (2024). Intrinsically disordered proteins studied by NMR spectroscopy. *J. Magn. Reson. Open* **18**, 100143. https://doi.org/10.1016/j.jmro.2023.100143.

[42]. Bolognesi, T., Schiavina, M., Felli, I.C., Pierattelli, R., (2025). NMR insights on multidomain proteins: the case of the SARS-CoV-2 nucleoprotein. *Prog. Nucl. Magn. Reson. Spectrosc.* **148–149**, 101577. https://doi.org/10.1016/j.pnmrs.2025.101577.

[43]. Korn, S.M., Lambertz, R., Fürtig, B., Hengesbach, M., Löhr, F., Richter, C., Schwalbe, H., Weigand, J.E., Wöhnert, J., Schlundt, A., (2021). ^{1}H, ^{13}C, and ^{15}N backbone chemical shift assignments of the C-terminal dimerization domain of SARS-CoV-2 nucleocapsid protein. *Biomol. NMR Assign.* **15**, 129–135. https://doi.org/10.1007/s12104-020-09995-y.

[44]. Zhou, R., Zeng, R., von Brunn, A., Lei, J., (2020). Structural characterization of the C-terminal domain of SARS-CoV-2 nucleocapsid protein. *Mol. Biomed.* **1**, 2. https://doi.org/10.1186/s43556-020-00001-4.

[45]. Caruso, I.P., dos Santos Almeida, V., do Amaral, M.J., de Andrade, G.C., de Araújo, G.R., de Araújo, T.S., de Azevedo, J.M., Barbosa, G.M., Bartkevihi, L., Bezerra, P. R., dos Santos Cabral, K.M., de Lourenço, I.O., Malizia-Motta, C.L.F., de Luna Marques, A., Mebus-Antunes, N. C., Neves-Martins, T.C., de Sá, J.M., Sanches, K., Santana-Silva, M.C., Vasconcelos, A.A., da Silva Almeida, M., de Amorim, G.C., Anobom, C.D., Da Poian, A.T., Gomes-Neto, F., Pinheiro, A.S., Almeida, F. C.L., (2022). Insights into the specificity for the interaction of the promiscuous SARS-CoV-2 nucleocapsid protein N-terminal domain with deoxyribonucleic acids. *Int. J. Biol. Macromol.* **203**, 466–480. https://doi.org/10.1016/j.ijbiomac.2022.01.121.

[46]. Korn, S.M., Dhamotharan, K., Jeffries, C.M., Schlundt, A., (2023). The preference signature of the SARS-CoV-2 nucleocapsid NTD for its 5′-genomic RNA elements. *Nature Commun.* **14**, 3331. https://doi.org/10.1038/s41467-023-38882-y.

[47]. Piai, A., Calçada, E.O., Tarenzi, T., del Grande, A., Varadi, M., Tompa, P., Felli, I.C., Pierattelli, R., (2016). Just a flexible linker? The structural and dynamic properties of CBP-ID4 revealed by NMR spectroscopy. *Biophys. J.* **110**, 372–381. https://doi.org/10.1016/j.bpj.2015.11.3516.

[48]. Sottini, A., Borgia, A., Borgia, M.B., Bugge, K., Nettels, D., Chowdhury, A., Heidarsson, P.O., Zosel, F., Best, R.B., Kragelund, B.B., Schuler, B., (2020). Polyelectrolyte interactions enable rapid association and dissociation in high-affinity disordered protein complexes. *Nature Commun.* **11**, 5736. https://doi.org/10.1038/s41467-020-18859-x.

[49]. Mantonico, M.V., De Leo, F., Quilici, G., Colley, L.S., De Marchis, F., Crippa, M., Mezzapelle, R., Schulte, T., Zucchelli, C., Pastorello, C., Carmeno, C., Caprioglio, F., Ricagno, S., Giachin, G., Ghitti, M., Bianchi, M.E., Musco, G., (2024). The acidic intrinsically disordered region of the inflammatory mediator HMGB1 mediates fuzzy interactions with CXCL12. *Nature Commun.* **15**, 1201. https://doi.org/10.1038/s41467-024-45505-7.

[50]. Fuxreiter, M., Tóth-Petróczy, Á., Kraut, D.A., Matouschek, A.T., Lim, R.Y.H., Xue, B., Kurgan, L., Uversky, V.N., (2014). Disordered proteinaceous machines. *Chem. Rev.* **114**, 6806–6843. https://doi.org/10.1021/cr4007329.

[51]. Arbesú, M., Pons, M., (2019). Integrating disorder in globular multidomain proteins: fuzzy sensors and the role of SH3 domains. *Arch. Biochem. Biophys.* **677**, 108161. https://doi.org/10.1016/j.abb.2019.108161.

[52]. Arbesú, M., Iruela, G., Fuentes, H., Teixeira, J.M.C., Pons, M., (2018). Intramolecular fuzzy interactions involving intrinsically disordered domains. *Front. Mol. Biosci.* **5** https://doi.org/10.3389/fmolb.2018.00039.

[53]. Beier, A., Schwarz, T.C., Kurzbach, D., Platzer, G., Tribuzio, F., Konrat, R., (2018). Modulation of correlated segment fluctuations in IDPs upon complex formation as an allosteric regulatory mechanism. *J. Mol. Biol.* **430**, 2439–2452. https://doi.org/10.1016/j.jmb.2018.04.035.

[54]. Kurzbach, D., Schwarz, T.C., Platzer, G., Höfler, S., Hinderberger, D., Konrat, R., (2014). Compensatory adaptations of structural dynamics in an intrinsically disordered protein complex. *Angew. Chem. Int. Ed.* **53**, 3840–3843. https://doi.org/10.1002/anie.201308389.

[55]. Cummings, R.D., Esko, J.D., (2022). Principles of Glycan Recognition. In: Varki, A., Cummings, R.D., Esko, J.D., Freeze, H.H., Stanley, P., Bertozzi, C.R., Hart, G.W., Etzler ME, M.E. (Eds.), *Essentials of Glycobiology*. Cold Spring Harbor Laboratory Press, Cold Spring Harbor (NY), pp. 387–402.

[56]. Weng, J., Wang, W., (2020). Dynamic multivalent interactions of intrinsically disordered proteins. *Curr. Opin. Struct. Biol.* **62**, 9–13. https://doi.org/10.1016/j.sbi.2019.11.001.

[57]. Sørensen, C.S., Jendroszek, A., Kjaergaard, M., (2019). Linker dependence of avidity in multivalent interactions between disordered proteins. *J. Mol. Biol.* **431**, 4784–4795. https://doi.org/10.1016/j.jmb.2019.09.001.

[58]. Borg, M., Mittag, T., Pawson, T., Tyers, M., Forman-Kay, J.D., Chan, H.S., (2007). Polyelectrostatic interactions of disordered ligands suggest a physical basis for ultrasensitivity. *PNAS* **104**, 9650–9655. https://doi.org/10.1073/pnas.0702580104.

[59]. Forsythe, H.M., Rodriguez Galvan, J., Yu, Z., Pinckney, S., Reardon, P., Cooley, R.B., Zhu, P., Rolland, A.D., Prell, Barbar, E., (2021). Multivalent binding of the partially disordered SARS-CoV-2 nucleocapsid phosphoprotein dimer to RNA. *Biophys. J.* **120**, 2890–2901. https://doi.org/10.1016/j.bpj.2021.03.023.

[60]. Bugge, K., Sottini, A., Ivanović, M.T., Buus, F.S., Saar, D., Fernandes, C.B., Kocher, F., Martinsen, J.H., Schuler, B., Best, R.B., Kragelund, B.B., (2025). Role of charges in a dynamic disordered complex between an IDP and a folded domain. *Nature Commun.* **16**, 3242. https://doi.org/10.1038/s41467-025-58374-5.

[61]. Csizmok, V., Follis, A.V., Kriwacki, R.W., Forman-Kay, J. D., (2016). Dynamic protein interaction networks and new structural paradigms in signaling. *Chem. Rev.* **116**, 6424–6462. https://doi.org/10.1021/acs.chemrev.5b00548.

[62]. López-Muñoz, A.D., Kosik, I., Holly, J., Yewdell, J.W., (2022). Cell surface SARS-CoV-2 nucleocapsid protein modulates innate and adaptive immunity. *Sci. Adv.* **8** https://doi.org/10.1126/sciadv.abp9770.

[63]. Clausen, T.M., Sandoval, D.R., Spliid, C.B., Pihl, J., Perrett, H.R., Painter, C.D., Narayanan, A., Majowicz, S. A., Kwong, E.M., McVicar, R.N., Thacker, B.E., Glass, C. A., Yang, Z., Torres, J.L., Golden, G.J., Bartels, P.L., Porell, R.N., Garretson, A.F., Laubach, L., Feldman, J., Yin, X., Pu, Y., Hauser, B.M., Caradonna, T.M., Kellman, B.P., Martino, C., Gordts, P.L.S.M., Chanda, S.K., Schmidt, A.G., Godula, K., Leibel, S.L., Jose, J., Corbett, K.D., Ward, A.B., Carlin, A.F., Esko, J.D., (2020). SARS-CoV-2 infection depends on cellular heparan sulfate and ACE2. *Cell* **183**, 1043–1057.e15. https://doi.org/10.1016/j.cell.2020.09.033.

[64]. Mycroft-West, C.J., Su, D., Pagani, I., Rudd, T.R., Elli, S., Gandhi, N.S., Guimond, S.E., Miller, G.J., Meneghetti, M. C.Z., Nader, H.B., Li, Y., Nunes, Q.M., Procter, P., Mancini, N., Clementi, M., Bisio, A., Forsyth, N.R., Ferro, V., Turnbull, J.E., Guerrini, M., Fernig, D.G., Vicenzi, E., Yates, E.A., Lima, M.A., Skidmore, M.A., (2020). Heparin inhibits cellular invasion by SARS-CoV-2: structural dependence of the interaction of the spike S1 receptor-binding domain with heparin. *Thromb. Haemost.* **120**, 1700–1715. https://doi.org/10.1055/s-0040-1721319.

[65]. Kim, S.Y., Jin, W., Sood, A., Montgomery, D.W., Grant, O.C., Fuster, M.M., Fu, L., Dordick, J.S., Woods, R.J., Zhang, F., Linhardt, R.J., (2020). Characterization of heparin and severe acute respiratory syndrome-related coronavirus 2 (SARS-CoV-2) spike glycoprotein binding interactions. *Antiviral Res.* **181**, 104873. https://doi.org/10.1016/j.antiviral.2020.104873.

[66]. Parafioriti, M., Ni, M., Petitou, M., Mycroft-West, C.J., Rudd, T.R., Gandhi, N.S., Ferro, V., Turnbull, J.E., Lima, M.A., Skidmore, M.A., Fernig, D.G., Yates, E.A., Bisio, A., Guerrini, M., Elli, S., (2023). Evidence for multiple binding modes in the initial contact between SARS-CoV-2 spike S1 protein and cell surface glycans. *Chem. Eur. J.* **29** https://doi.org/10.1002/chem.202202599.

[67]. Froese, J., Mandalari, M., Civera, M., Elli, S., Pagani, I., Vicenzi, E., Garcia-Monge, I., Di Iorio, D., Frank, S., Bisio, A., Lenhart, D., Gruber, R., Yates, E.A., Richter, R.P., Guerrini, M., Wegner, S.V., Grobe, K., (2024). Evolution of SARS-CoV-2 spike trimers towards optimized heparan sulfate cross-linking and inter-chain mobility. *Sci. Rep.* **14**, 32174. https://doi.org/10.1038/s41598-024-84276-5.

[68]. Marley, J., Lu, M., Bracken, C., (2001). A method for efficient isotopic labeling of recombinant proteins. *J.*

Biomol. NMR **20**, 71–75. https://doi.org/10.1023/A:1011254402785.

[69]. Solyom, Z., Schwarten, M., Geist, L., Konrat, R., Willbold, D., Brutscher, B., (2013). BEST-TROSY experiments for time-efficient sequential resonance assignment of large disordered proteins. *J. Biomol. NMR* **55**, 311–321. https://doi.org/10.1007/s10858-013-9715-0.

[70]. Lescop, E., Schanda, P., Brutscher, B., (2007). A set of BEST triple-resonance experiments for time-optimized protein resonance assignment. *J. Magn. Reson.* **187**, 163–169. https://doi.org/10.1016/j.jmr.2007.04.002.

[71]. Bermel, W., Bertini, I., Csizmok, V., Felli, I.C., Pierattelli, R., Tompa, P., (2009). H-start for exclusively heteronuclear NMR spectroscopy: the case of intrinsically disordered proteins. *J. Magn. Reson.* **198**, 275–281. https://doi.org/10.1016/j.jmr.2009.02.012.

[72]. Bermel, W., Bertini, I., Duma, L., Felli, I.C., Emsley, L., Pierattelli, R., Vasos, P.R., (2005). Complete assignment of heteronuclear protein resonances by protonless NMR spectroscopy. *Angew. Chem. Int. Ed.* **44**, 3089–3092. https://doi.org/10.1002/anie.200461794.

[73]. Felli, I.C., Pierattelli, R., (2015). Spin-state-selective methods in solution- and solid-state biomolecular ^{13}C NMR. *Prog. Nucl. Magn. Reson. Spectrosc.* **84–85**, 1–13. https://doi.org/10.1016/j.pnmrs.2014.10.001.

[74]. Pontoriero, L., Schiavina, M., Murrali, M.G., Pierattelli, R., Felli, I.C., (2020). Monitoring the interaction of α-synuclein with calcium ions through exclusively heteronuclear nuclear magnetic resonance experiments. *Angew. Chem. Int. Ed.* **59**, 18537–18545. https://doi.org/10.1002/anie.202008079.

[75]. Schiavina, M., Bracaglia, L., Rodella, M.A., Kümmerle, R., Konrat, R., Felli, I.C., Pierattelli, R., (2023). Optimal ^{13}C NMR investigation of intrinsically disordered proteins at 1.2 GHz. *Nature Protoc.* **19**, 406–440. https://doi.org/10.1038/s41596-023-00921-9.

[76]. Slad, S., Bermel, W., Kümmerle, R., Mathieu, D., Luy, B., (2022). Band-selective universal 90° and 180° rotation pulses covering the aliphatic carbon chemical shift range for triple resonance experiments on 1.2 GHz spectrometers. *J. Biomol. NMR* **76**, 185–195. https://doi.org/10.1007/s10858-022-00404-1.

[77]. Geen, H., Freeman, R., (1991). Band-selective radiofrequency pulses. *J. Magn. Reson.* **93**, 93–141. https://doi.org/10.1016/0022-2364(91)90034-Q.

[78]. Bohlen, J.-M., Rey, M., Bodenhausen, G., (1989). Refocusing with chirped pulses for broadband excitation without phase dispersion. *J. Magn. Reson.* **84**, 191–197. https://doi.org/10.1016/0022-2364(89)90018-8.

[79]. Shaka, A.J., Keeler, J., Frenkiel, T., Freeman, R., (1983). An improved sequence for broadband decoupling: WALTZ-16. *J. Magn. Reson.* **52**, 335–338. https://doi.org/10.1016/0022-2364(83)90207-X.

[80]. Grzesiek, S., Bax, A., (1992). Improved 3D triple-resonance NMR techniques applied to a 31 kDa protein. *J. Magn. Reson.* **96**, 432–440. https://doi.org/10.1016/0022-2364(92)90099-S.

[81]. Kay, L.E., Ikura, M., Tschudin, R., Bax, A., (1990). Three-dimensional triple-resonance NMR spectroscopy of isotopically enriched proteins. *J. Magn. Reson.* **89**, 496–514. https://doi.org/10.1016/0022-2364(90)90333-5.

[82]. Clubb, R.T., Thanabal, V., Wagner, G., (1992). A constant-time three-dimensional triple-resonance pulse scheme to correlate intraresidue ^{1}HN, ^{15}N, and $^{13}C'$ chemical shifts in ^{15}N ^{13}C-labelled proteins. *J. Magn. Reson.* **97**, 213–217. https://doi.org/10.1016/0022-2364(92)90252-3.

[83]. Grzesiek, S., Bax, A., (1993). Amino acid type determination in the sequential assignment procedure of uniformly $^{13}C/^{15}N$-enriched proteins. *J. Biomol. NMR* **3**, 185–204. https://doi.org/10.1007/BF00178261.

[84]. Kupce, E., Freeman, R., (1993). Polychromatic selective pulses. *J. Magn. Reson. A* **102**, 122–126. https://doi.org/10.1006/jmra.1993.1079.

[85]. Lescop, E., Kern, T., Brutscher, B., (2010). Guidelines for the use of band-selective radiofrequency pulses in heteronuclear NMR: example of longitudinal-relaxation-enhanced BEST-type $^{1}H–^{15}N$ correlation experiments. *J. Magn. Reson.* **203**, 190–198. https://doi.org/10.1016/j.jmr.2009.12.001.

[86]. Markley, J.L., Bax, A., Arata, Y., Hilbers, C.W., Kaptein, R., Sykes, B.D., Wright, P.E., Wüthrich, K., (1998). Recommendations for the presentation of NMR structures of proteins and nucleic acids – IUPAC-IUBMB-IUPAB Inter-Union task group on the standardization of databases of protein and nucleic acid structures determined by NMR spectroscopy. *J. Biomol. NMR* **12**, 1–23. https://doi.org/10.1023/A:1008290618449.

[87]. Keller, R., (2004). The Computer Aided Resonance Assignment Tutorial. CANTINA Verlag, Zurich.

[88]. Williamson, M.P., (2013). Using chemical shift perturbation to characterise ligand binding. *Prog. Nucl. Magn. Reson. Spectrosc.* **73**, 1–16. https://doi.org/10.1016/j.pnmrs.2013.02.001.

[89]. Morris, G.M., Huey, R., Lindstrom, W., Sanner, M.F., Belew, R.K., Goodsell, D.S., Olson, A.J., (2009). AutoDock4 and AutoDockTools4: Automated docking with selective receptor flexibility. *J. Comput. Chem.* **30**, 2785–2791. https://doi.org/10.1002/jcc.21256.

[90]. Case, D.A., Cheatham, T.E., Darden, T., Gohlke, H., Luo, R., Merz, K.M., Onufriev, A., Simmerling, C., Wang, B., Woods, R.J., (2005). The Amber biomolecular simulation programs. *J. Comput. Chem.* **26**, 1668–1688. https://doi.org/10.1002/jcc.20290.

[91]. Kirschner, K.N., Yongye, A.B., Tschampel, S.M., González-Outeiriño, J., Daniels, C.R., Foley, B.L., Woods, R.J., (2008). GLYCAM06: a generalizable biomolecular force field. Carbohydrates. *J. Comput. Chem.* **29**, 622–655. https://doi.org/10.1002/jcc.20820.

[92]. Jorgensen, W.L., Chandrasekhar, J., Madura, J.D., Impey, R.W., Klein, M.L., (1983). Comparison of simple potential functions for simulating liquid water. *J. Chem. Phys.* **79**, 926–935. https://doi.org/10.1063/1.445869.

[93]. Phillips, J.C., Braun, R., Wang, W., Gumbart, J., Tajkhorshid, E., Villa, E., Chipot, C., Skeel, R.D., Kalé, L., Schulten, K., (2005). Scalable molecular dynamics with NAMD. *J. Comput. Chem.* **26**, 1781–1802. https://doi.org/10.1002/jcc.20289.

[94]. Humphrey, W., Dalke, A., Schulten, K., (1996). VMD: Visual molecular dynamics. *J. Mol. Graph.* **14**, 33–38. https://doi.org/10.1016/0263-7855(96)00018-5.